Modeling of Turbulent Flow Past a Circular Cylinder Using Large Eddy Simulation on Unstructured Grids

Orxan Şibliyev

Submitted to the
Institute of Graduate Studies and Research
in partial fulfillment of the requirements for the Degree of

Master of Science
in
Mechanical Engineering

Eastern Mediterranean University
August 2012
Gazimağusa, North Cyprus

Approval of the Institute of Graduate Studies and Research

Prof. Dr. Elvan Yılmaz
Director

I certify that this thesis satisfies the requirements as a thesis for the degree of Master of Science in Mechanical Engineering.

Assoc. Prof. Dr. Uğur Atikol
Chair, Department of Mechanical Engineering

We certify that we have read this thesis and that in our opinion it is fully adequate in scope and quality as a thesis for the degree of Master of Science in Mechanical Engineering.

Prof. Dr. İbrahim Sezai
Supervisor

Examining Committee

1. Prof. Dr. İbrahim Sezai
2. Assoc. Prof. Dr. Fuat Egelioğlu
3. Assist. Prof. Dr. Hasan Hacışevki

ABSTRACT

In this work, a computer program is written for solving the turbulent flow equations on unstructured grids using a Large Eddy Simulation (LES) model in C++ language. To test the code, two cases are considered: laminar, periodic flow past a circular cylinder at Reynolds number, Re_D = 100 which is based on the diameter of the cylinder and turbulent flow at Re_D = 3900. The turbulence or sub-grid scale (SGS) model is chosen as Smagorinsky model due to its simplicity compared with dynamic models. It was found that, for the laminar case, drag, lift, and back-pressure coefficients, pressure and velocities matched quite well with the reference values obtained from literature. For the turbulent case of Re_D = 3900, there is some discrepancy between the results of the present investigation and the results obtained from other resources which is due to rather coarse grid distribution dictated by the insufficient computing resources.

Keywords: Computational fluid dynamics, circular cylinder, large eddy simulation, unstructured mesh, turbulence

ÖZ

Piyasada Hesaplamalı Akışkanlar Dinamiği (HAD) problemlerini çözmek için bazı ticari yazılımlar olsa da, ana denklemleri ve onların ayrışımlarını, türbülans modellemesini, programlamayı ve diğer HAD ile ilgili meseleleri derinlemesine anlamak için bireysel olarak yazımış bir yazılıma ihtiyaç vardur. Bu tezde, bu amaçlanmıştır ve ek olarak, yazılım, şekilsiz ızgaraları da çözecek şekilde, kapsamlı bir biçimde yazılmaya çalışılmıştır. Kodu test etmek için, iki durum düşünülmüştür; Reynolds sayısı, Re_D = 100' de laminar, periodik dairesel silindir üzerinden geçen akış, ve aynı problem ama bu kez Re_D = 3900'de türbülans bir akış ile ve türbülans modeli olarak Smagorinsky Büyük Eddy Simulasyonu (BES) kullanılarak. Gösterilmiştir ki, laminar durum referans veri ile karşılaştırınca, engel, kaldırma ve basınç katsayıları, anlık basınç alanı kontür çizimi, ve ortalama akışa bakılarak, hiçbir sorun olmadan çalışmıştır. Diğer yandan, Re_D = 3900 durumu yine aynı parametlere bakılarak ama bu defa ek olarak, sürtünme katsayısı, türbülans statistikleri ve daha birçok parametre ile test edilmiştir. Re_D = 100 durumunda olduğu gibi, bu durumda da sonuçların çoğu referans değerlerle uyuşuyor. Bazı değerlerle ise referans değerler arasında ufak farklılıklar vardır. Bunun nedeni ise göreceli olarak daha düşük çözünürlükte ızgara kullanmaktır.

Anahtar kelimeler: Hesaplamalı akışkanlar dinamiği, dairesel silindir, büyük eddy simulasyonu, düzensiz ızgara, türbülans

ACKNOWLEDGEMENTS

First of all, I would like to thank to my supervisor Prof. Dr. İbrahim Sezai very much because he taught me not only those valuable courses, supervised me, and helped me with technical problems but also he taught me how to be endlessly patient.

For being my thesis committee members, I thank Assoc. Prof. Dr. Fuat Egelioğlu, Assoc. Prof. Dr. Uğur Atikol, and Assist. Prof. Dr. Hasan Hacışevki.

No doubt, I would not be able to write even a word for the thesis without the support of my family so, I am thankful to them. I especially want to thank to my nephew Tuğra, who will be a great tennis player in the future, being my source of motivation.

I also want to thank Assist. Prof. Dr. Rasime Uyguroğlu for allowing me to work on the workstation she provided.

TABLE OF CONTENTS

LIST OF TABLES

LIST OF FIGURES

NOMENCLATURE

Upper-case Roman

A	Area	[m^2]	
A_p	Planform area	[m^2]	
C_d	Drag coefficient		$\frac{F_x}{p_\mathrm{dyn}}$
C_f	Friction coefficient		$\frac{\tau_w}{p_\mathrm{dyn}}$
C_l	Lift coefficient		$\frac{F_y}{p_\mathrm{dyn}}$
C_p	Pressure coefficient		$\frac{p-p_\infty}{p_\mathrm{dyn}}$
C_pb	Back-pressure coefficient		$\frac{p-p_\infty}{p_\mathrm{dyn}}$
C_SGS	Sub-grid scale constant		
D	Diameter of cylinder	[m]	
R	Residual		
Re	Reynolds number		
Re_D	Reynolds number based on diameter		$\frac{U_\infty D}{\nu}$
S	Strain rate	[1/s]	
St	Strouhal number		$\frac{fD}{U_\infty}$
V	Volume	[m^3]	
U_∞	Free stream velocity	[m/s]	

Lower-case Roman

$\dot{m}$	Mass flow rate	[kg/s]
a	Coefficient in FV discretized equation	
$\mathbf{e}$	Cartesian coordinates unit vector	
nb	Neighbour	
$\mathrm{n_c}$	Number of cells	
$\mathrm{n_f}$	Number of faces	
p	Pressure	[Pa]
p^m	Modified pressure	[Pa]
s	Source term	
t	Time	[s]
$\mathbf{v}$	Cartesian velocity vector	[m/s]
v_∞	Free stream velocity	[m/s]
x	Streamwise Cartesian coordinate	[m]

y	Cross-stream Cartesian coordinate	[m]	
z	Spanwise Cartesian coordinate	[m]	
f	Vortex shedding frequency	1/s	$1/\tau_w$
p_{dyn}	Dynamic pressure	[Pa]	$\frac{1}{2}\rho U_\infty^2 A_{\text{p}}$

Upper-case Greek

Δ	Filter cutoff width	[m]
Δt	Temporal increment	[s]

Lower-case Greek

μ	Molecular dynamic viscosity	[Pa.s]
μ_{SGS}	Dynamic SGS viscosity	[Pa.s]
α	Geometric interpolation factor	
α_{p}	Pressure under-relaxation factor	
δ	Kronecker delta	
θ_{sep}	Seperation angle	[degree]
ν	Kinematic viscosity	[m^2/s]
ν_{SGS}	Kinematic SGS viscosity	[m^2/s]
τ	SGS stress	[Pa]
τ_p	Period	[s]
τ_{wall}	Wall shear stress	[Pa]
ϕ	Conserved passive scalar	
ρ	Density	[kg/m^3]

Abbreviations

BC	Boundary condition
CD	Central difference
CFD	Computational fluid dynamics
CV	Control volume
DNS	Direct Numerical Simulation
EFD	Experimental fluid dynamics
FLOP	Floating point operations
FV	Finite volume
LES	Large eddy simulation
LHS	Left hand side
MIM	Momentum Interpolation Method
RANS	Reynolds-Averaged Navier-Stokes
RHS	Right hand side
SGS	Sub-grid scale

Subscripts

d,l	Drag, Lift
eff	Effective
f	Face
i,j,k	Suffix notation indices

Superscripts

ϕ^{t-1}	Value of ϕ in previous time step
ϕ^{n-1}	Value of ϕ in previous iteration
ϕ^{*}	Guessed ϕ
ϕ^{c}	Correction of ϕ
ϕ'	Fluctuation of ϕ
$\overline{\phi}$	Filtered ϕ
dc	Deferred correction
H	Higher-order
pres	Pressure
trans	Transient
U	Upwind

Symbols

∇	Gradient operator
$\nabla\cdot$	Divergence operator
max(a,b)	The greater of a and b
min(a,b)	The lesser of a and b

Chapter 1

INTRODUCTION

1.1. Introduction

Computational fluid dynamics or CFD is the analysis of systems involving fluid flow, heat transfer and associated phenomena such as chemical reactions by means of computer-based simulation [1]. The reason to prefer CFD over experimental fluid dynamics (EFD) is that former is easier to prepare and use. For every simulation, a different experimental setup is required whereas this is not the case for a computer. Moreover, there is no concern of the quality, maintenance and the price of experimental instruments. On the other hand, for CFD, only a workstation is required. The initial cost of a workstation may be high if many nodes are employed to work in parallel however; still it is advantageous compared to EFD considering the long usage of workstation. To mention a drawback of CFD, for high Reynolds number flows CFD is impractical since very fine spatial and temporal resolutions are required so, increasing the simulation time drastically.

There are vast amount of fields that CFD could be applied such as multiphase flow, combustion modeling, turbulence modeling and so on. Turbulence modeling is one of the important areas since it occurs in most of the real-world flows such as atmospheric flows and in engineering/industrial flows. Contrary to laminar flow, turbulence is characterized with random motions with small time and length scales depending on Reynolds number. Intensity of turbulence determines the model to be

used. For low Reynolds numbers all flow structures could be solved by Direct Numerical Simulation (DNS) which is a no-model method. However, for higher Reynolds number flows which are point of interest, turbulence modeling must be implemented. In turbulence models for Reynolds Averaged Navier-Stokes (RANS) equations, all length scales are modeled and this allows mesh to be coarser compared with DNS, but on the other hand, lacks accuracy. An intermediate solution is LES in which only small-scale motions are modeled whereas large-scale motions (large eddies) are solved exactly. Since small eddies exhibit more universal behavior than large eddies which are geometry dependent, accuracy of results are better than models for RANS equations.

Since turbulence occurs in most of the practical flows, one of its applications is flow over a cylinder in any shape but rectangular and circular are the most common geometries. Rectangular cylinder is somewhat less complex compared with circular one due to its sharp edges. On the other hand, circular cylinder is rich in flow structures such as boundary layers, shear layers, separation and reattachment, vertical structures, etc. So, circular cylinder provides a better opportunity for testing of the code. Flow over a cylinder has many practical applications such as submarines, off shore structures, bridge piers, pipelines, etc. [2]. In the literature, there are several experimental [3, 4, 5] and numerical results [6, 7, 8, 9, 2, 10, 11] for the study of flow around a cylinder over a range of Reynolds number, both laminar and turbulent flows. For turbulent flows, Re_D = 3900 (D is the diameter of the cylinder) case is probably the more documented one in the literature due to its practical resemblances [9]. So, it would be logical to analyze Re_D = 3900 to make comparisons with sufficient amount of data.

On the other hand, to show that the code is working correctly, a $Re_D = 100$ is also tested. This case is helpful since the flow is laminar and it takes little time to obtain the results whereas $Re_D = 3900$ case takes a lot of time.

The computer code, which is written in C++, is able solve unstructured meshes (although in this work a structured mesh is utilized) and written using finite volume (FV) method. Making the code generic so that it would be capable of working on unstructured grids is important in order to understand CFD in many aspects including programming. Moreover, working with unstructured grids is advantageous because in this case complex and limited curvilinear method is avoided.

Thus, the aim of this thesis is two-fold; firstly, it aims to validate the self-made computer code and to test its ability to capture the complex structures in the flow. Secondly, to leave a reference with its discrepancies to be improved for an MS student who is interested in this subject.

1.2. Organization of Thesis

Chapter 2 describes some important physical phenomena such as energy cascade and Kolmogorov's hypotheses and characteristic regions of flow field for a flow over circular cylinder.

In chapter 3, the followed methodology explained. First of all, filtering operation is discussed in order to apply to governing equations. Then, along with SGS model governing equations for LES are presented and subsequently, the discretization of

those governing equations is shown. Having discretized transport equation, numerical parameters, physical domain and the numerical mesh and accordingly the treatment of boundary conditions are presented.

In chapter 4 and 5, results are presented and discussed and the conclusions are drawn, respectively.

Chapter 2

LITERATURE REVIEW

Literature review shows that self-made solvers have been used in many seminal papers ([6, 7, 8, 9, 10, 11, 12]). Self-made solvers mean that the codes are not commercial since they are open and/or academic solvers developed by the authors or department for academic purposes. As is evident from the mentioned references in which self-made codes have been used, it is beneficial not to use commercial codes. This is because using a commercial code prevents possible modifications on the code and it also may work slower than a self-made code. Specifically, for a thesis, a self-made code is required because application of the theory requires a hands-on practice to allow having a better insight into the theory.

Pertaining the validation cases, it was observed that the case of flow over a circular cylinder at $Re_D = 100$ has been studied by some authors such as by [2] and [13]. In these sources, there is a strong agreement on the results obtained. Some of these results are mean drag coefficient, mean back-pressure coefficient, and Strouhal number. Due to the strong agreement between the studies, it could be said that this case has been solved completely. Being a trustful validation case, this case was also used in the present work.

For another validation case where $Re_D = 3900$, there have been a vast amount of studies ([6, 7, 8, 9, 10, 11, 12, 14, 15]) with LES. This choice of Reynolds number

seems to be optimal as a validation case because for higher Reynolds number flows, simulation time increases dramatically due to higher spatial and temporal resolutions. Another case in which Re_D = 1000, could also be studied; however, the number of studies on Re_D = 3900 is higher than on Re_D = 1000. Hence, Re_D = 3900 case is more suitable to have abundant number of data to compare the present results with. As a turbulence model, most of the time LES was preferred in the literature; but LES, DES, and RANS were used by [16] and also a comparison of RANS and LES was made by [17].

Parnaudeau et al. ([9]) studied flow over a circular cylinder at Re_D = 3900 and analyzed the flow both numerically with LES and experimentally with hot-wire anemometry and particle image velocimetry (PIV). High-order schemes and also an immersed boundary method were used for the numerical simulation. They investigated the turbulence statistics and the power spectra in the near wake (up to 10 diameters).

Kravchenko and Moin ([10]), also studied the flow over circular cylinder at Re_D = 3900 using LES. They used a high-order accurate numerical method based on *B*-splines. Additionally, they investigated the impact of the grid resolution on the shear layer transition. Near the cylinder, their findings matched well with experimental findings of [5]. Since the findings of [5] are limited with the near wake region, for the far wake region (6*D* to 10*D*), the results were compared with the findings of [4]. One of most important findings of their work is about the effect of grid resolution and domain length in spanwise direction on the solution of the problem. They concluded that insufficient grid resolution can result in early transition in the shear

layers which separates from the cylinder. This causes inaccuracy in the solution of the problem.

Not only the case of Re_D = 3900 but also Re_D = 140000 was studied by Fröhlich et al. [11] by using both structured and unstructured grids. For the structured grid, they used finite volume approach by using a specialized code for LES, while for the unstructured grid they used finite volume approach. Then they compared the results of the structured and the unstructured grid cases with each other and also with the results obtained in the literature. It is concluded that in the comparison of structured and unstructured grid cases, the cost of the simulation in terms of time passed were the same. However, for the unstructured grid case, the wake region was not resolved accurately. Also they resulted in that structured grids have the disadvantage of having unnecessary points in certain areas while for unstructured grids the knowledge on where fine resolution is required to be known in advance.

Mahesh et al. ([6]) carried out several simulations one of which was on Re_D = 3900 case with LES. They used an unstructured grid and clustered the nodes in the boundary layer and the wake.

Franke and Frank ([12]), studied a LES of Re_D = 3900 case with cell-centered finite volume approach and compared the results with DNS results of Ma et al. ([18]) and experimental results of Ong and Wallace ([4]). Also, they analyzed the turbulence statistics. Their results were well matched with the DNS results of [18] and experimental results of [4] for the near wake region.

Flow over a circular cylinder at Re_D = 3900 was also studied by Breuer ([8]) by using LES. He used five different convective flux schemes and compared them with each other. It is concluded that central difference schemes of 2^{nd} and 4^{th} orders were well suited for LES however, upwind-biased schemes were not recommended. Moreover, he analyzed the influence of different grid resolutions and SGS model on the solution. Both Smagorinsky and dynamic models were used in that work. To observe the effect of SGS model better, simulations were al performed without a SGS-model.

Beaudan and Moin ([14]), performed a LES of Re_D = 3900 case by using both Smagorinsky and dynamic SGS models. They used high-order accurate upwind-biased methods and analyzed the turbulent wake behind a circular cylinder. Temporal resolution was of 2^{nd} order and the formulation was fully implicit.

In addition to the analysis of flow a single circular cylinder at Re_D = 3900, Afgan et al. ([7]), studied two side-by-side cylinders as well by using dynamic SGS model. Then based on length of the domain in spanwise direction, grid resolution near the wall, convection scheme, and the SGS model, a sensitivity analysis was carried out. They analyzed both mean and instantaneous flow quantities and also turbulence statistics. They found that the mean pressure coefficient, recirculation length, separation angle and the Strouhal number were well agreed with available DNS and experimental results.

As can be seen, both the Smagorinsky and the dynamic models were used in the literature and it was found that dynamic model results in higher accuracy compared

to Smagorinsky model. Also, most of the time, finite volume approach was preferred as in the present work. Both structured and unstructured grid topologies were tested although generally structured grids were the main choice. In the present work, the self-made code is developed to work on unstructured grids however; a structured grid was preferred to have a better control on the grid topology. To obtain accurate results, in all of the sources and this work as well, 2^{nd} or higher-order spatial and temporal discretization was utilized.

Chapter 3

PHYSICAL ASPECTS

3.1. Energy Cascade and Kolmogorov's Hypothesis

In a turbulent flow, there are motions with a wide range of scales. According to Richardson [19] as cited in [20], in an *energy cascade*, kinetic energy is transferred from large scales of motion to smaller ones successively until the energy is dissipated by viscous forces. Kolmogorov made important hypotheses based on this energy cascade. According to Kolmogorov's hypothesis [21] of local isotropy as cited in [20], the small-scale turbulent motions are statistically isotropic at sufficiently high Reynolds number. In page 184 of reference [20] it is continued as

> Just as the directional information of the large scales is lost as the energy passes down the cascade, Kolmogorov argued that all information about the geometry of the large eddies – determined by the mean flow field and boundary conditions – is also lost. As a consequence, the statistics of the small-scale motions are in a sense universal – similar in every high Reynolds number turbulent flow.

Since small-scale motions are universal at high-Reynolds number flows, small-scales could be modeled whereas large-scales could be solved exactly, hence the acronym Large Eddy Simulation.

3.2. Regions of Flow Field

For circular cylinder problem, domain can be divided into regions which are incoming flow; boundary layer, wake region, and shear layer (see Figure 1).

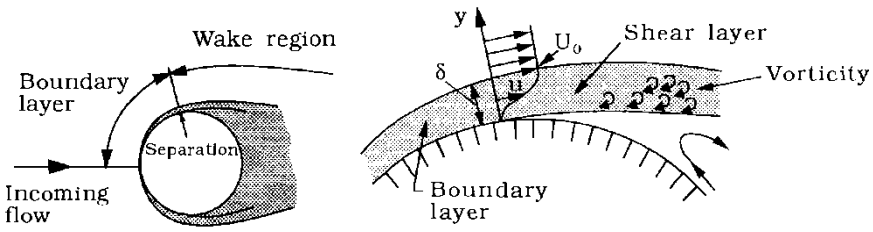

Figure 1: Regions of flow (left), Shear layer (right) [22]

Location of transition to turbulence depends on Re_D ($u_\infty D/\nu$) (see Table 1). Considering θ =0° as stagnation point where incoming flow hits (see Figure 1a), there is a positive (favorable) pressure gradient initially however, after a certain point, due to the presence of another stagnation point at θ =180°, adverse pressure gradient occurs causing flow adjacent to cylinder to rotate and eventually flow separates from cylinder.

Table 1: State of flow according to Reynolds number

Reynolds number	**State of flow**
0 < Re < 180-200	Laminar
180-200 < Re < 350-400	Tr. in wake
350-400 < Re < 100,000-200,000	Tr. in shear layers or subcritical state
100,000-200,000 < Re < unknown	Tr. in boundary layers or critical state

Up to Re = 40, flow is steady and two symmetric, counter-rotating vortices arise behind the cylinder, in the recirculation zone, in the wake. After Re = 40, flow becomes sensitive to disturbances and eventually becomes unsteady and a well-

known phenomenon, vortex shedding or Von Kármán street (see Figure 2), occurs in the wake. The vortex shedding mechanism initiates with faster growth of one of the pair of vortices and counter-rotation of vortices triggers that faster growing vortex to shed from the recirculation zone. Subsequently, another vortex sheds and this process repeats until transition to turbulence take place in the wake, at far downstream. As Re increases, transition region moves towards upstream. Further increase in Re causes transition to initiate in shear layers while boundary layer and flow separation is still laminar and this regime is termed as subcritical regime (350-400 < Re < 100,000-200,000). It is called subcritical for boundary layer, meaning transition to turbulence has not initiated in boundary layers yet [23]. Subsequently, critical regime follows and then all flow around cylinder becomes turbulent.

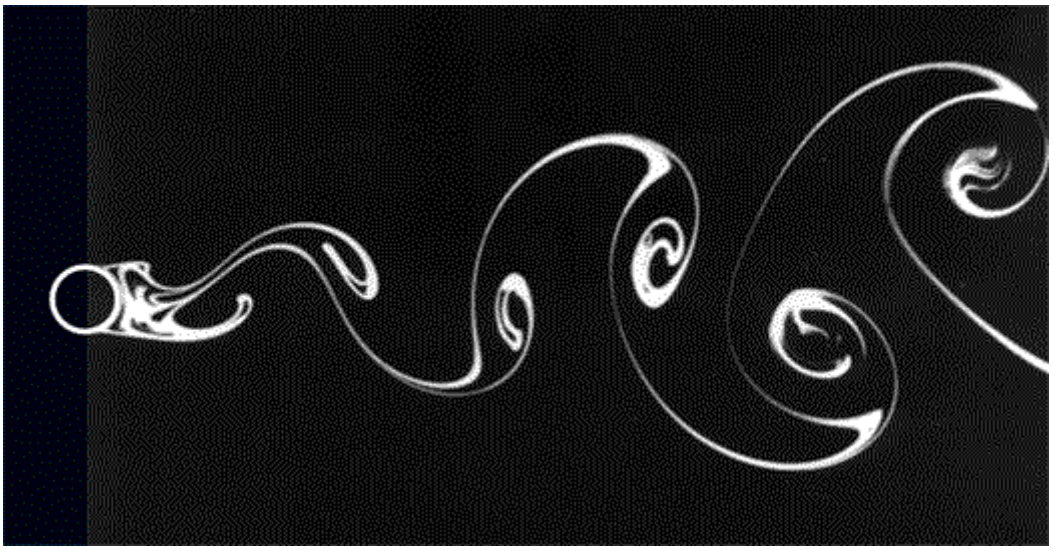

Figure 2: Von Kármán street [45]

Chapter 4

METHODOLOGY

4.1. Filtering

An instantaneous velocity field is split as resolved (large eddy) and unresolved or sub-filter (small eddy) as in eq (4.1).

$$v_i = \overline{v}_i + v_i' \tag{4.1}$$

where, $\overline{v}_i$ is the resolved part while v_i' is the unresolved part. Note that, resolved and unresolved parts are denoted with an over-bar and a prime, respectively. To obtain resolved flow field a filtering operation can be carried out as shown below [1].

$$\overline{\phi}(\mathbf{x},t) = \int_{-\infty}^{\infty}\int_{-\infty}^{\infty}\int_{-\infty}^{\infty} G(\mathbf{x},\mathbf{x}',\Delta)\phi(\mathbf{x}',t)\,\mathrm{d}x_1'\mathrm{d}x_2'\mathrm{d}x_3' \tag{4.2}$$

where G is the filter function, $\overline{\phi}(\mathbf{x},t)$ is the filtered variable ϕ is the unfiltered variable, and Δ is the filter cutoff width.

After filtering operation, fluctuations of the velocity field will be ironed out. This could be understood by comparing LES and DNS as depicted in Figure 3. There are several filter functions such as Gaussian, spectral cutoff, and top-hat or box filter. The top-hat filter, which is shown in eq. (4.3), is commonly used for FV implementations of LES [1] and is also preferred in this thesis. This filtering operation is not carried out in time as is the case for RANS but in 3D space. Filter cutoff width Δ, determines what length scales would be filtered. It is convenient

to take it as cubic root of grid cell volume (see eq. (4.4)) but not smaller than that since scales smaller than grid cell volume cannot be solved anyway. Cutoff width affects governing equations through SGS viscosity which will be described later.

$$G(\mathbf{x},\mathbf{x}',\Delta)=\begin{cases}1/\Delta^3 & |\mathbf{x}-\mathbf{x}'|\le\Delta/2\\ 0 & |\mathbf{x}-\mathbf{x}'|>\Delta/2\end{cases} \tag{4.3}$$

$$\Delta = V^{1/3} \tag{4.4}$$

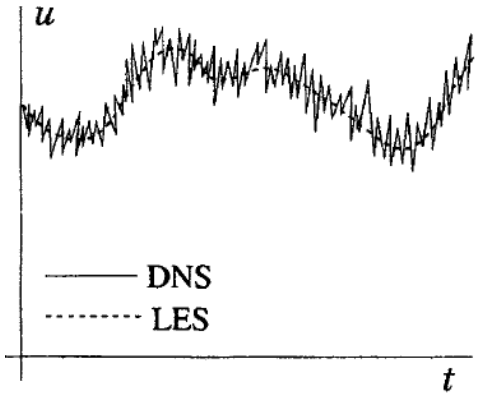

Figure 3: Velocity history at a point, comparison of LES and DNS [24]

4.2. Governing Equations

In this section, along with continuity and momentum equations for LES, SGS model will be presented. Materials in this section are adapted from [25].

4.2.1. Continuity Equation

Filtered, incompressible continuity equation states that divergence of the resolved velocity field is zero such as:

$$\frac{\partial \overline{v}_i}{\partial x_i} = 0 \tag{4.5}$$

4.2.2. Momentum Equations

Navier-Stokes equation for a Newtonian fluid is:

$$\rho\frac{\partial v_i}{\partial t}+\rho\frac{\partial}{\partial x_j}\left(v_i v_j\right)+\frac{\partial p}{\partial x_i}=\mu\frac{\partial}{\partial x_j}\left(\frac{\partial v_i}{\partial x_j}+\frac{\partial v_j}{\partial x_i}\right) \tag{4.6}$$

Filtering of eq. (4.6) with the filtering operation defined in eq. (4.2) using top-hat function (eq. (4.3)) yields:

$$\rho\frac{\partial \overline{v}_i}{\partial t}+\rho\frac{\partial}{\partial x_j}\left(\overline{v_i v_j}\right)+\frac{\partial \overline{p}}{\partial x_i}=\mu\frac{\partial}{\partial x_j}\left(\frac{\partial \overline{v}_i}{\partial x_j}+\frac{\partial \overline{v}_j}{\partial x_i}\right) \tag{4.7}$$

In addition to filtered variables, eq. (4.7) involves a variable which is $\overline{v_i v_j}$. Instead of this form, it is written as follows:

$$\frac{\partial}{\partial x_j}\left(\overline{v_i v_j}\right)=\frac{\partial}{\partial x_j}\left(\overline{v}_i\overline{v}_j\right)+\frac{\partial}{\partial x_j}\left(\overline{v_i v_j}-\overline{v}_i\overline{v}_j\right) \tag{4.8}$$

Substituting the equation above into eq. (4.7) yields:

$$\rho\frac{\partial \overline{v}_i}{\partial t}+\rho\frac{\partial}{\partial x_j}\left(\overline{v}_i\overline{v}_j\right)+\frac{\partial \overline{p}}{\partial x_i}=\mu\frac{\partial}{\partial x_j}\left(\frac{\partial \overline{v}_i}{\partial x_j}+\frac{\partial \overline{v}_j}{\partial x_i}\right)+\rho\frac{\partial}{\partial x_j}\left(\overline{v_i v_j}-\overline{v}_i\overline{v}_j\right) \tag{4.9}$$

The presence of the last term on RHS is due to the filtering operation and it is the divergence of SGS stress tensor, τ which represents the effect of SGS stresses onto the resolved flow field and it is defined as follows:

$$\tau=\rho\begin{bmatrix}\left(\overline{v_1 v_1}-\overline{v}_1\overline{v}_1\right) & \left(\overline{v_2 v_1}-\overline{v}_2\overline{v}_1\right) & \left(\overline{v_3 v_1}-\overline{v}_3\overline{v}_1\right)\\ \left(\overline{v_1 v_2}-\overline{v}_1\overline{v}_2\right) & \left(\overline{v_2 v_2}-\overline{v}_2\overline{v}_2\right) & \left(\overline{v_3 v_2}-\overline{v}_3\overline{v}_2\right)\\ \left(\overline{v_1 v_3}-\overline{v}_1\overline{v}_3\right) & \left(\overline{v_2 v_3}-\overline{v}_1\overline{v}_3\right) & \left(\overline{v_3 v_3}-\overline{v}_3\overline{v}_3\right)\end{bmatrix} \tag{4.10}$$

So with the definition above, it is clear that:

$$\rho \frac{\partial}{\partial x_j}\left(\overline{v_i v_j} - \overline{v}_i \overline{v}_j\right) = \frac{\partial \tau_{ij}}{\partial x_j} \tag{4.11}$$

Substituting the equation above into eq. (4.9) yields:

$$\rho \frac{\partial \overline{v}_i}{\partial t} + \rho \frac{\partial}{\partial x_j}\left(\overline{v}_i \overline{v}_j\right) + \frac{\partial \overline{p}}{\partial x_i} = \frac{\partial}{\partial x_j}\left[\mu\left(\frac{\partial \overline{v}_i}{\partial x_j} + \frac{\partial \overline{v}_j}{\partial x_i}\right) - \tau_{ij}\right] \tag{4.12}$$

τ could be split into three parts using the decomposition in eq. (4.1) (see [1] for details). Hence,

$$\tau_{ij} = \rho\left(\overline{\overline{v}_i \overline{v}_j} - \overline{v}_i \overline{v}_j\right) + \rho\left(\overline{\overline{v}_i v_j'} + \overline{v_i' \overline{v}_j}\right) + \rho \overline{v_i' v_j'} \tag{4.13}$$

In the equation above, the first term is called Leonard stresses, the second term is called cross-stresses, and the last term is called LES Reynolds stresses. In page 102 of [1] their physical meanings are explained as follows:

> The Leonard stresses are solely due to effects at resolved scale. They are caused by the fact that a second filtering operation makes a change to a filtered flow variable… The cross-stresses are due to interactions between the SGS eddies and the resolved flow… Finally, the LES Reynolds stresses are caused by convective momentum transfer due to interactions of SGS eddies and are modeled with a so-called SGS turbulence model.

Instead of modeling Reynolds stresses, in [26] as cited in [1], it is noted that in current versions of the FV method, although the nature of Leonard stresses and cross-stress are different, they could be lumped together with the Reynolds stresses

or in other words, contributions of Leonard and cross-stresses are neglected. SGS stresses could be approximated by using Bouissnesq approximation which relates SGS stresses to the resolved flow via dynamic SGS viscosity μ_{SGS} as shown in the following eq. (4.14). Note that, the second term in is required to ensure that normal SGS stresses to be equal to turbulent kinetic energy.

$$\begin{aligned}\tau_{ij} &= -\mu_{\text{SGS}}\left(\frac{\partial \overline{v}_i}{\partial x_j}+\frac{\partial \overline{v}_j}{\partial x_i}\right)+\frac{1}{3}\tau_{ii}\delta_{ij} \\ &= -2\mu_{\text{SGS}}\overline{S}_{ij}+\frac{1}{3}\tau_{ii}\delta_{ii}\end{aligned} \tag{4.14}$$

where $\overline{S}_{ij}$ is the strain rate of the resolved flow field and is defined as:

$$\overline{S}_{ij}=\frac{1}{2}\left(\frac{\partial \overline{v}_i}{\partial x_j}+\frac{\partial \overline{v}_j}{\partial x_i}\right) \tag{4.15}$$

Substituting eq. (4.14) into eq. (4.12) and with some regrouping:

$$\rho\frac{\partial \overline{v}_i}{\partial t}+\rho\frac{\partial}{\partial x_j}\left(\overline{v}_i\overline{v}_j\right)+\frac{\partial \overline{p}}{\partial x_i}=\frac{\partial}{\partial x_j}\left[\left(\mu+\mu_{\text{SGS}}\right)\left(\frac{\partial \overline{v}_i}{\partial x_j}+\frac{\partial \overline{v}_j}{\partial x_i}\right)-\frac{1}{3}\tau_{ii}\delta_{ij}\right] \tag{4.16}$$

In eq. (4.16), a modified pressure p^{m} can be defined by common factoring the pressure and the last term in parenthesis on LHS which is the trace of stress tensor such as:

$$\frac{\partial \overline{p}}{\partial x_i}+\frac{1}{3}\frac{\partial}{\partial x_i}\left(\tau_{ii}\delta_{ij}\right)=\frac{\partial}{\partial x_i}\left(\overline{p}+\frac{1}{3}\tau_{ii}\delta_{ij}\right)=\frac{\partial p^{\text{m}}}{\partial x_i} \tag{4.17}$$

Although pressure is modified it will be denoted as $\overline{p}$ hereon. Defining $\mu_{\text{eff}}=\mu+\mu_{\text{SGS}}$ and substituting the definition of modified pressure into eq. (4.16) yields:

$$\rho\frac{\partial\overline{v}_i}{\partial t}+\rho\frac{\partial}{\partial x_j}\left(\overline{v}_i\overline{v}_j\right)+\frac{\partial\overline{p}}{\partial x_i}=\frac{\partial}{\partial x_j}\left[\mu_{\text{eff}}\left(\frac{\partial\overline{v}_i}{\partial x_j}+\frac{\partial\overline{v}_j}{\partial x_i}\right)\right] \tag{4.18}$$

The RHS of eq. (4.18) can be expanded as:

$$\begin{aligned}\frac{\partial}{\partial x_j}\left[\mu_{\text{eff}}\left(\frac{\partial\overline{v}_i}{\partial x_j}+\frac{\partial\overline{v}_j}{\partial x_i}\right)\right]&=\frac{\partial}{\partial x_j}\left[\mu_{\text{eff}}\frac{\partial\overline{v}_i}{\partial x_j}\right]+\frac{\partial}{\partial x_j}\left[\mu_{\text{eff}}\frac{\partial\overline{v}_j}{\partial x_i}\right]\\&=\frac{\partial}{\partial x_j}\left[\mu_{\text{eff}}\frac{\partial\overline{v}_i}{\partial x_j}\right]\\&\quad+\frac{\partial}{\partial x_j}\left(\mu_{\text{SGS}}\frac{\partial\overline{v}_j}{\partial x_i}\right)+\mu\frac{\partial}{\partial x_j}\frac{\partial\overline{v}_j}{\partial x_i}\end{aligned} \tag{4.19}$$

In recognition of that fact that molecular viscosity is space independent, if $\overline{u}$ has continuous second order partial derivatives (Clairaut's or Schwarz's theorem), then order of derivative could be changed such as:

$$\frac{\partial}{\partial x_j}\frac{\partial\overline{v}_j}{\partial x_i}=\frac{\partial}{\partial x_i}\frac{\partial\overline{v}_j}{\partial x_j}=0 \tag{4.20}$$

The equation above is zero due to continuity equation. Therefore eq. (4.18) is written as:

$$\rho\frac{\partial\overline{v}_i}{\partial t}+\rho\frac{\partial}{\partial x_j}\left(\overline{v}_i\overline{v}_j\right)+\frac{\partial\overline{p}}{\partial x_i}=\frac{\partial}{\partial x_j}\left[\mu_{\text{eff}}\frac{\partial\overline{v}_i}{\partial x_j}\right]+\frac{\partial}{\partial x_j}\left(\mu_{\text{SGS}}\frac{\partial\overline{v}_j}{\partial x_i}\right) \tag{4.21}$$

The pressure term and the last term on the RHS shall be treated as source terms. As a result, ultimate form of momentum equation is obtained as:

$$\rho\frac{\partial\overline{v}_i}{\partial t}+\rho\frac{\partial}{\partial x_j}\left(\overline{v}_i\overline{v}_j\right)=\frac{\partial}{\partial x_j}\left(\mu_{\text{eff}}\frac{\partial\overline{v}_i}{\partial x_j}\right)+s_i \tag{4.22}$$

where,

$$s_i = \frac{\partial}{\partial x_j}\left(\mu_{\text{SGS}} \frac{\partial \overline{v}_j}{\partial x_i}\right) - \frac{\partial \overline{p}}{\partial x_i} \tag{4.23}$$

4.2.3. SGS Model

There are several SGS models such as Smagorinsky model [27], mixed model [28], dynamic model [29]. SM, which is preferred in this thesis, is an eddy viscosity model. The eddy viscosity or, in this context, SGS viscosity, as mentioned before, causes increased dissipation and this is one of the effects of unresolved flow field onto resolved one. This is expected in the concept of energy cascade stating kinetic energy is progressively transferred to smaller eddies which perform work against the action of viscous stresses, so that the energy associated with small-scale eddy motions is dissipated and converted into thermal internal energy. Besides dissipative nature, smallest eddies are involved in transport of fluid as well.

SM builds on Prandtl's mixing length model for which it is assumed that kinematic SGS viscosity ($\nu_{\text{SGS}} = \mu_{\text{SGS}} / \rho$) can be described in terms of one length scale and one velocity scale. Denoting length scale as Kolmogorov length scale η and velocity scale as Kolmogorov velocity scale u_η, SGS kinematic viscosity can be written as:

$$\nu_{\text{SGS}} = \text{C}_1 \eta u_\eta \tag{4.24}$$

Velocity scale can be obtained assuming that Re is high enough hence; rate of production of turbulent kinetic energy is approximately equal to its rate of

dissipation. Production term can be obtained from governing equation for mean flow kinetic energy or turbulent kinetic energy and it is,

$$\mathrm{P} = 2\nu_{\mathrm{SGS}} S_{ij} S_{ij} \tag{4.25}$$

where, $S_{ij}S_{ij}$ is a scalar product of two tensors such that,

$$S_{ij}S_{ij} = \sum_{i=1}^{3}\sum_{j=1}^{3} S_{ij}^{\,2} \tag{4.26}$$

On the other hand, using Kolmogorov scales rate of dissipation scales as:

$$\varepsilon = \frac{u_\eta^{\,3}}{\eta} \tag{4.27}$$

Equating the production term to the rate of dissipation one can obtain,

$$2\mathrm{C}_1 \eta u_\eta S_{ij} S_{ij} = \frac{u_\eta^{\,3}}{\eta} \Rightarrow u_\eta = \mathrm{C}_2 \eta \sqrt{2S_{ij}S_{ij}} \tag{4.28}$$

Now, SGS kinematic viscosity can be written as:

$$\nu_{\mathrm{SGS}} = \left(\mathrm{C}_{\mathrm{SGS}}\eta\right)^2 \sqrt{2S_{ij}S_{ij}} \tag{4.29}$$

where $\mathrm{C}_{\mathrm{SGS}}$ is the SGS constant. SGS viscosity should diminish as the distance to the wall becomes smaller since there could be no turbulence near the wall. To achieve this, SGS constant could be multiplied by a damping factor. In this thesis a damping function which is used in [30] is utilized as shown below (another possibility is the Van Driest damping).

$$f = \sqrt{1 - \exp\left(-n^+ / A\right)^3} \tag{4.30}$$

where n^+ which is defined below is the non-dimensional distance from the cylinder surface and A is 25.

$$n^+ = \frac{n v_\tau}{\nu} \quad \text{where} \quad \mathrm{v}_\tau = \sqrt{\frac{\tau}{\rho}} \tag{4.31}$$

Note that in the equation above, n is the dimensional distance from the cylinder wall and v_τ is the shear velocity. Also, it is convenient to set length scale to filter cut-off width, therefore,

$$\eta = \Delta = V^{1/3} \tag{4.32}$$

As a result, SGS dynamic viscosity can be written as:

$$\mu_{\text{SGS}} = \rho\left(C_{\text{SGS}}\Delta f\right)^2 \sqrt{2S_{ij}S_{ij}} \tag{4.33}$$

One of the disadvantages of the SM is that the SGS constant is problem-specific, that is, it is not universal. There have been several attempts to determine SGS constant [31, 32, 33, 34] and it turned out that its value varies between approximately 0.1 and 0.2 although 0.065 was tested as well by [14]. In this thesis, it is taken as 0.065 as well.

4.3. Discretization

In the following sub-sections discretization of continuity and momentum equations will be presented and at the end, general transport equation will be obtained. Majority of the materials are adapted from [25].

4.3.1. Continuity Equation

In accordance with FV method, integrating eq. (4.5) over a CV yields:

$$\int_{\text{CV}} \frac{\partial \overline{v}_i}{\partial x_i} \mathrm{d}V = 0 \tag{4.34}$$

Now it is required to utilize Gauss's divergence theorem. For a vector **a**, theorem states that,

$$\int_{\mathrm{CV}} \nabla \cdot \mathbf{a} \mathrm{d}V = \oint_{A} \mathbf{n} \cdot \mathbf{a} \mathrm{d}V \tag{4.35}$$

where n is the unit vector normal to area A.

Applying eq. (4.35) to the continuity equation yields:

$$\oint_{A} \overline{v}_i \cdot \mathrm{dA}_i \approx \sum_{f=1}^{\mathrm{n_f}} \left(\overline{v}_i \cdot \mathrm{A}_i \right)_f = \sum_{f=1}^{\mathrm{n_f}} \dot{m}_f = 0 \tag{4.36}$$

4.3.2. Momentum Equations

Integration of eq. (4.22) over CV yields:

$$\rho \int_{\mathrm{CV}} \frac{\partial \left(\overline{v}_i \right)}{\partial t} \mathrm{d}V + \rho \int_{\mathrm{CV}} \frac{\partial \overline{v}_i \overline{v}_j}{\partial x_j} \mathrm{d}V = \int_{\mathrm{CV}} \frac{\partial}{\partial x_j} \left(\mu_{\mathrm{eff}} \frac{\partial \overline{v}_i}{\partial x_j} \right) \mathrm{d}V + \int_{\mathrm{CV}} s_i \mathrm{d}V \tag{4.37}$$

Applying Gauss's divergence theorem (eq. (4.35)) to the equation above yields:

$$\underbrace{\rho \frac{\partial}{\partial t} \int_{\mathrm{CV}} \overline{\mathrm{v}}_i \mathrm{d}V}_{\text{Transient term}} + \underbrace{\rho \oint_{\mathrm{A}} \overline{v}_i \overline{v}_j \mathrm{d}A_j}_{\text{Convective term}} = \underbrace{\oint_{\mathrm{A}} \mu_{\mathrm{eff}} \frac{\partial \overline{v}_i}{\partial x_j} \mathrm{d}A_j}_{\text{Diffusion term}} + \underbrace{\int_{\mathrm{CV}} s_i \mathrm{d}V}_{\text{Source term}} \tag{4.38}$$

In the following sub-sections, discretization of each term will be shown.

4.3.2.1. Transient Term

The 2nd order accurate, three time level temporal discretization is used such that (see Figure 4),

$$\rho \frac{\partial}{\partial t} \int_{\mathrm{CV}} \overline{\mathrm{v}}_i \mathrm{d}V \approx \rho V \frac{3\overline{\mathrm{v}}_{i,P}^{\mathrm{t}} - 4\overline{\mathrm{v}}_{i,P}^{\mathrm{t-1}} + \overline{\mathrm{v}}_{i,P}^{\mathrm{t-2}}}{2\Delta t} \tag{4.39}$$

The second term will be treated as a source term such that,

$$s_i^{\text{trans}} = a_P^{\text{trans}} \left(\frac{4}{3} \overline{\mathrm{v}}_{i,P}^{\,t-1} + \frac{1}{3} \overline{\mathrm{v}}_{i,P}^{\,t-2} \right) \tag{4.40}$$

where,

$$a_P^{\text{trans}} = \frac{3}{2} \frac{\rho V}{\Delta t} \tag{4.41}$$

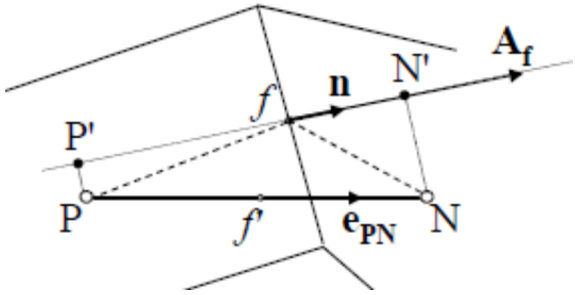

Figure 4: Sketch of geometric parameters [25]

4.3.2.2. Convective Term

The convection term is approximated as:

$$\rho \oint_{\mathrm{A}} \overline{v}_i \overline{v}_j \mathrm{d}A_j \approx \rho \sum_{f=1}^{\mathrm{n_f}} \left(\overline{v}_i \overline{v}_j A_j \right)_f = \sum_{f=1}^{\mathrm{n_f}} \dot{m}_f \overline{v}_{i,f} \tag{4.42}$$

To calculate mass flow rate, $\dot{m}_f$, the velocity at cell face, $\overline{v}_{i,f}$, should be calculated using the Momentum Interpolation Method (MIM) of Rhie and Chow [35] in order to avoid checkerboard pressure field for co-located grid arrangement. The derivation of MIM for unstructured grids is in Appendix B.

The cell face velocity is interpolated with CD scheme which is of 2nd order accurate and it is preferred over upwind-biased schemes due to their intrinsic dissipative

nature which causes excessive dissipation when combined with SGS viscosity. According to [36], I2 interpolation criterion is utilized.

Defining interpolation factor as (see Figure 4):

$$\alpha = \frac{\mathbf{Pf} \cdot \mathbf{e}_{PN}}{\left(\mathbf{PN} \cdot \mathbf{PN}\right)^{1/2}} \tag{4.43}$$

The cell face velocity can be found as:

$$\overline{v}_{i,f} = \overline{v}_{i,f^*} + \left(\nabla \overline{\mathbf{v}}\right)_{f^*} \cdot \mathbf{f}^* \mathbf{f} \tag{4.44}$$

where, $\nabla \overline{v}_{i,f^*} = \left(1-\alpha\right)\nabla \overline{v}_{i,P} + \alpha \nabla \overline{v}_{i,N}$. The second term in eq. (4.44) is treated as a source term.

To make the code to be able to compare different convective schemes, deferred correction approach is utilized. As a result, the cell face value is implemented as the sum of the cell face variable which is found by 1st order upwind scheme and the difference of a higher order scheme and again the 1st order scheme which are evaluated at the previous iteration as shown below.

$$\overline{v}_{i,f} = \overline{v}^{\mathrm{U}}_{i,f} + \left(\overline{v}^{\mathrm{H}}_{i,f} - \overline{v}^{\mathrm{U}}_{i,f}\right)^{\mathrm{n}-1} \tag{4.45}$$

where,

$\overline{v}^{\mathrm{U}}_{i,f}$ is the cell face value computed by 1st order upwind method

$\overline{v}^{\mathrm{H}}_{i,f}$ is the cell face value computed by a higher order scheme

Note that the second term which belongs to the previous iteration acts as a (deferred) corrector of the 1st order upwind scheme. It will be diminished as the problem converges to a solution.

For the 1st order upwind scheme,

$$\begin{aligned} \overline{v}_{i,f} &= \overline{v}_{i,P} \quad \text{if} \quad \dot{m}_f > 0 \\ \overline{v}_{i,f} &= \overline{v}_{i,N} \quad \text{if} \quad \dot{m}_f < 0 \end{aligned} \tag{4.46}$$

Hence, $\overline{v}_i^{f,\mathrm{U}} = \max\left(\dot{m}_f, 0\right)\overline{v}_{i,P} - \min\left(\dot{m}_f, 0\right)\overline{v}_{i,N}$.

On other hand, regarding higher order scheme, in page 340 of [36] criterion I2 which is shown below will be used (see Figure 4).

$$\overline{v}_{i,f} = \overline{v}_{i,f'} + \left(\nabla\overline{\mathbf{v}}\right)_{f'} \cdot \mathbf{f'f} \tag{4.47}$$

In order to obtain the components of the equation above, a central difference (CD) scheme is utilized instead of upwind schemes due to their intrinsic dissipative nature which would cause excessive dissipation by having increased viscosity effect. Hence,

$$\begin{aligned} \overline{v}_{i,f^*} &= \left(1-\alpha\right)\overline{v}_{i,P} + \alpha\overline{v}_{i,N} \\ \left(\nabla\overline{\mathbf{v}}\right)_{f^*} &= \left(1-\alpha\right)\left(\nabla\overline{\mathbf{v}}\right)_P + \alpha\left(\nabla\overline{\mathbf{v}}\right)_N \end{aligned} \tag{4.48}$$

As a result, the discretized convection term is:

$$\sum_{f=1}^{\mathrm{n_f}} \dot{m}_f \overline{v}_{i,f} = \underbrace{\sum_{f=1}^{\mathrm{n_f}} \dot{m}_f \overline{v}_i^{f,\mathrm{U}}}_{\text{implicit}} + \underbrace{\dot{m}_f^{\mathrm{n-1}}\left(\overline{v}_{i,f}^{\mathrm{H}} - \overline{v}_i^{f,\mathrm{U}}\right)^{\mathrm{n-1}}}_{\text{explicit}} \tag{4.49}$$

where the explicit term is treated as a source term s_i^{dc}. The superscript *dc* denotes that deferred correction approach is utilized. Again, note that the explicit term acts as a corrector of the implicit term. Thus,

$$s_i^{\mathrm{dc}} = \dot{m}_f \left(\overline{v}_{i,f}^{\mathrm{H}} - \overline{v}_i^{f,\mathrm{U}} \right)^{\mathrm{n}-1} \tag{4.50}$$

4.3.2.3. Diffusion Term

The diffusion term is approximated as:

$$\oint_{\mathrm{A}} \mu_{\mathrm{eff}} \frac{\partial \overline{v}_i}{\partial x_j} \mathrm{d}A_j \approx \sum_{f=1}^{\mathrm{n_f}} \left(\mu_{\mathrm{eff}} \frac{\partial \overline{v}_i}{\partial x_j} A_j \right)_f \tag{4.51}$$

$\frac{\partial \overline{v}_i}{\partial x_j} A_j$ could be split into orthogonal and non-orthogonal (cross-diffusion) components such as (see Figure 4):

$$\frac{\partial \overline{v}_i}{\partial x_j} A_j \approx \frac{\overline{v}_{i,N'} - \overline{v}_{i,P'}}{\mathbf{PN} \cdot \mathbf{n}_f} A_f = \frac{\overline{v}_{i,N'} - \overline{v}_{i,P'}}{\left|\mathbf{PN}\right| \mathbf{e}_{PN} \cdot \mathbf{n}_f} A_f = \frac{\overline{v}_{i,N'} - \overline{v}_{i,P'}}{\left|\mathbf{PN}\right|} A_f^{PN} \tag{4.52}$$

where A_f^{PN} is the component of A_f in the direction of line PN and it is defined as:

$$A_f^{PN} = \frac{A_f}{\mathbf{e}_{\mathrm{PN}} \cdot \mathbf{n}_f} \tag{4.53}$$

Also as seen from Figure 4,

$$\begin{aligned} \overline{v}_{i,P'} &\approx \overline{v}_{i,P} + \left(\nabla \overline{\mathbf{v}}\right)_P \cdot \mathbf{PP'} \\ \overline{v}_{i,N'} &\approx \overline{v}_{i,N} + \left(\nabla \overline{\mathbf{v}}\right)_N \cdot \mathbf{NN'} \end{aligned} \tag{4.54}$$

Applying the changes to eq. (4.52) yields:

$$\frac{\partial \overline{v}_i}{\partial x_j} A_j = \underbrace{\frac{\overline{v}_{i,N} - \overline{v}_{i,P}}{|\mathbf{PN}|} A_f^{PN}}_{\text{orthogonal term}} + \underbrace{\frac{\left(\nabla \overline{v}_i\right)_N \cdot \mathbf{NN'} - \left(\nabla \overline{v}_i\right)_P \cdot \mathbf{PP'}}{|\mathbf{PN}|} A_f^{PN}}_{\text{non-orthogonal term}} \tag{4.55}$$

The second term is treated as a source term as s_i^{cd}. The superscript *cd* denotes "cross-diffusion". Hence,

$$s_i^{\text{cd}} = \frac{\left(\nabla \overline{v}_i\right)_N \cdot \mathbf{NN'} - \left(\nabla \overline{v}_i\right)_P \cdot \mathbf{PP'}}{|\mathbf{PN}|} A_f^{PN} \tag{4.56}$$

As a result, the discretized diffusion term is:

$$\sum_{f=1}^{\text{n}_\text{f}} \left(\mu_{\text{eff}} \frac{\partial \overline{v}_i}{\partial x_j} A_j \right)_f = \sum_{f=1}^{\text{n}_\text{f}} \left(\mu_{\text{eff},f} \frac{\overline{v}_{i,N} - \overline{v}_{i,P}}{|\mathbf{PN}|} A_f^{PN} \right) + s_i^{\text{cd}} \tag{4.57}$$

4.3.2.4. Source Term

Source term is discretized as:

$$\int_{\text{CV}} s_i \text{d}V = s_i V \tag{4.58}$$

There are four contributions to the source term which are,

$$s_i = s_i^{\text{trans}} + s_i^{\text{dc}} + s_i^{\text{cd}} + s_i^{\text{pres}} + s_i^{\text{SGS}} \tag{4.59}$$

Transient s_i^{trans}, deferred correction s_i^{dc}, and the cross-diffusion s_i^{cd} source terms are defined with equations (4.40), (4.50), and (4.56), respectively. The two other terms, s_i^{pres} and s_i^{SGS} will be discretized in this section.

Pressure source term is discretized as follows:

$$s_i^{\text{pres}} = -\frac{\partial p}{\partial x_i} V = -\sum_{f=1}^{\text{n}_\text{f}} \left(p A_i \right)_f \tag{4.60}$$

Another term, SGS source term is discretized by using Gauss's divergence theorem (eq. (4.35)) such as:

$$s_i^{\text{SGS}} = \int_{\text{CV}} \frac{\partial}{\partial x_j} \left(\mu_{\text{SGS}} \frac{\partial v_j}{\partial x_i} \right) \text{d}V = \oint_A \left(\mu_{\text{SGS}} \frac{\partial \overline{v}_j}{\partial x_i} \text{d}A_j \right) \approx \sum_{f=1}^{\text{n}_\text{f}} \left(\mu_{\text{SGS}} \frac{\partial \overline{v}_j}{\partial x_i} A_j \right)_f \tag{4.61}$$

Note that, the term $\frac{\partial \overline{v}_j}{\partial x_i} A_j$ is equal to the i$^{\text{th}}$ component of dot product of the tensor of gradient of velocity field and area vector. Explicitly,

$$\frac{\partial \overline{v}_j}{\partial x_i} A_j = \left(\nabla \mathbf{v} \cdot \mathbf{A} \right)_i \tag{4.62}$$

4.3.3. Discretized Transport Equation

Substituting the discretized forms of the transient, convection, and diffusion terms into eq. (4.38), the discretized transport equation is obtained as:

$$a_P \overline{v}_{i,P} = \sum_{N=\text{nb}(P)} a_N \overline{v}_{i,N} + s_i \tag{4.63}$$

where, s_i is given in eq. (4.59) and

$$\begin{aligned} a_N &= \frac{\mu_{\text{eff}} A_f^{PN}}{\left| \mathbf{PN} \right|} - \min\left(\dot{m}_f, 0 \right) \\ a_P &= \sum_{N=\text{nb}(P)} a_N + a_P^{\text{t-1}} \end{aligned} \tag{4.64}$$

4.4. Numerical and Computational Details

For Re = 100, time step is 0.1 seconds, simulation duration is 200 seconds, and averaging start time is 150^{th} second. On the other hand, for Re = 3900, time step is 0.001 seconds, simulation duration is 40 seconds, and averaging start time is 25^{th} second.

The algorithm used is SIMPLE which is suitable for LES if the time step is small enough. Refer to Appendix B for the derivation of SIMPLE algorithm for unstructured grids. Since a collocated arrangement is utilized, to avoid checker-board pressure field Rhie and Chow's MIM [35] (see Appendix A for the derivation for unstructured grids) is used. The under-relaxation factor of the pressure correction is 0.3. Both momentum and pressure correction equations are solved with Gauss-Seidel method. Momentum equations are solved once per inner iteration since they are non-linear whereas pressure correction equation is repeated eight times. It should be mentioned that, the usage of conjugate gradient method would allow faster convergence compared to Gauss-Seidel however, its parallel application is left for future works. To mention, the initial values of velocities and pressure is zero.

As a gradient reconstruction method, the least-squares method ([37]) is used instead of iterative Gauss's method ([25]).

Maximum number of inner iterations in a time step is fixed at a value of 10 if the residuals defined by eq. (4.65). There is a possibility that residuals defined by eq. (4.65) may not drop below the tolerance which is set to $5x10^{-5}$ at the initial stage of

the simulation. However, this does not pose any problem since early flow field data is not point of interest.

$$R_i = \frac{\sum_{\mathrm{n_c}} \left| \sum_{N=\mathrm{nb}(P)} a_N \overline{v}_{i,N} + s_i - a_P \overline{v}_{i,P} \right|}{\sum_{\mathrm{n_c}} \left| \sum_{N=\mathrm{nb}(P)} a_P \overline{v}_{i,P} \right|} \tag{4.65}$$

The code is parallelized using the domain decomposition technique among eight threads of a HP Z800 workstation, whose processor specifications are shown in Table 2. Since the memory type is shared memory, openMP ([38]) is used to divide the work among the threads.

Since in this work software libraries such as LINPACK or LAPACK are not used for matrix/vector calculations, FLOP rate cannot be given. However, it is recorded that every iteration takes one second after a certain time (about 2 seconds).

Table 2: Processor specifications

Model	Intel(R) Xeon(R) E5530
Speed	2.40 GHz
RAM	3.98 GB

4.5. Physical Domain and Mesh

4.5.1. Introduction

In the following sub-sections, specifications of the physical domains and meshes for two validations cases will be discussed.

4.5.2. Case 1: $Re_D = 3900$

The front and top views of the physical domain are shown in Figure 5 and Figure 6, respectively, together with the boundary conditions. The numerical mesh which is block-structured is shown in Figure 7 and a closer view at the intersection of blocks is shown in Figure 8. The dimensions of the physical domain are completely identical to the that of reference [12] which is given in page 1197.

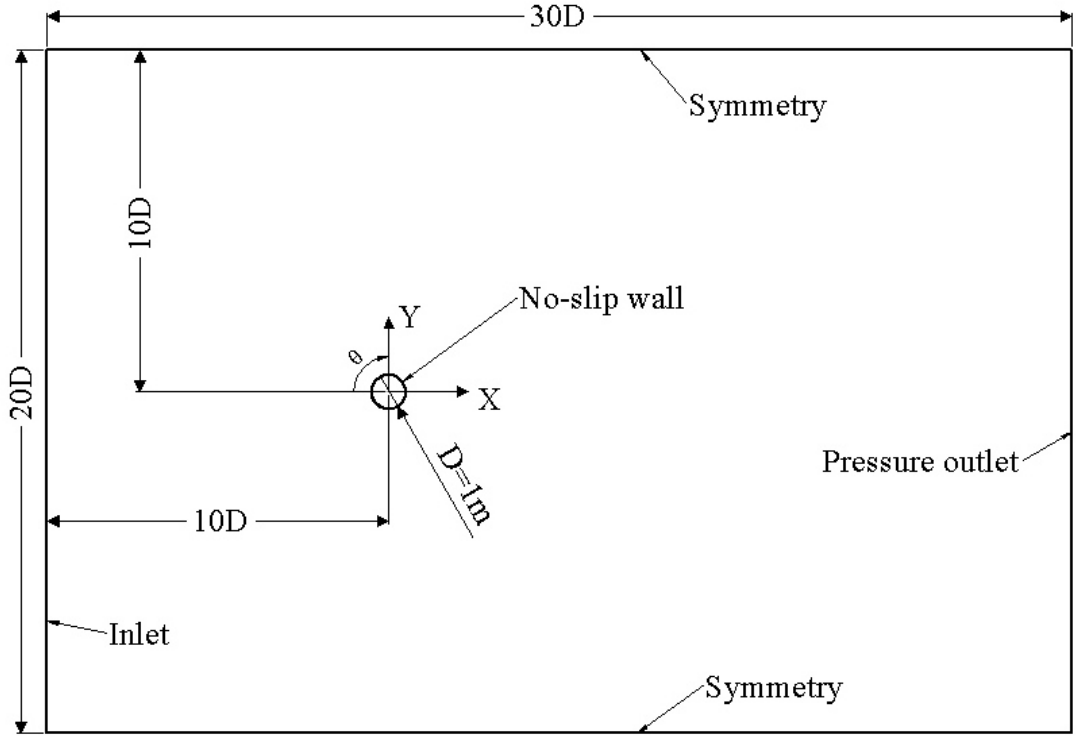

Figure 5: Front view of the physical domain

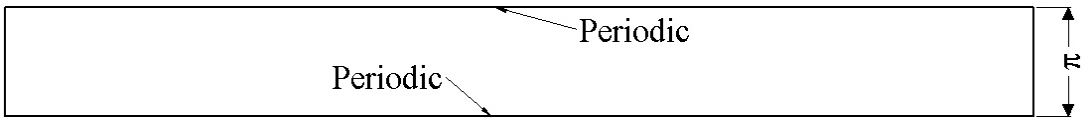

Figure 6: Top view of the physical domain

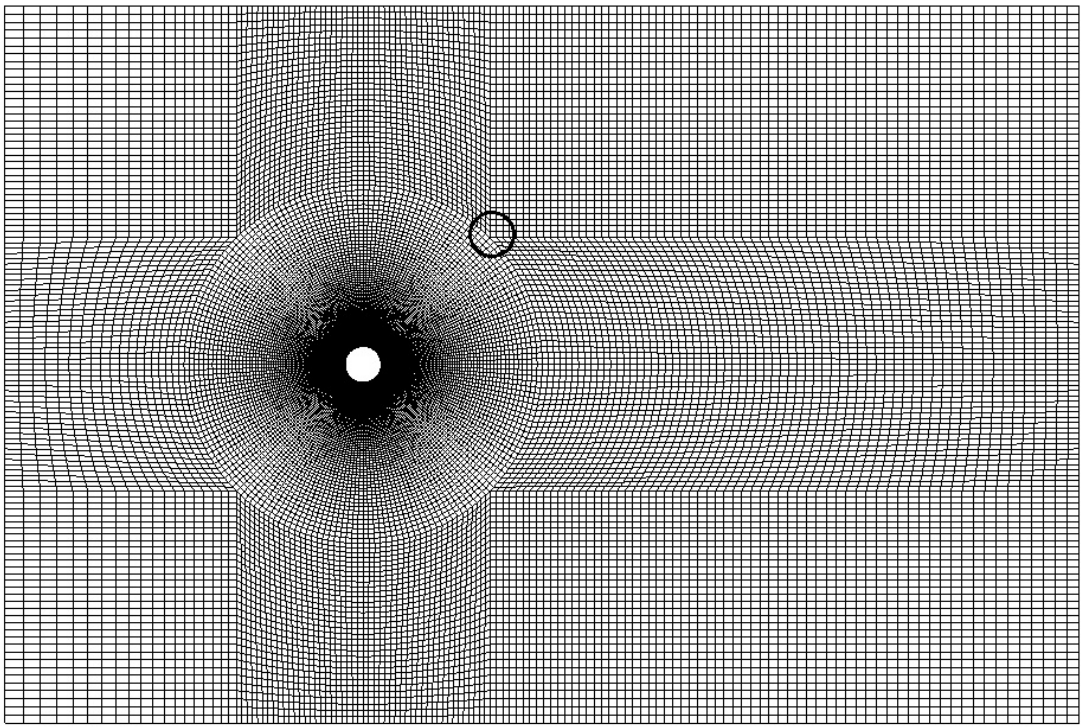

Figure 7: 2D view of numerical mesh

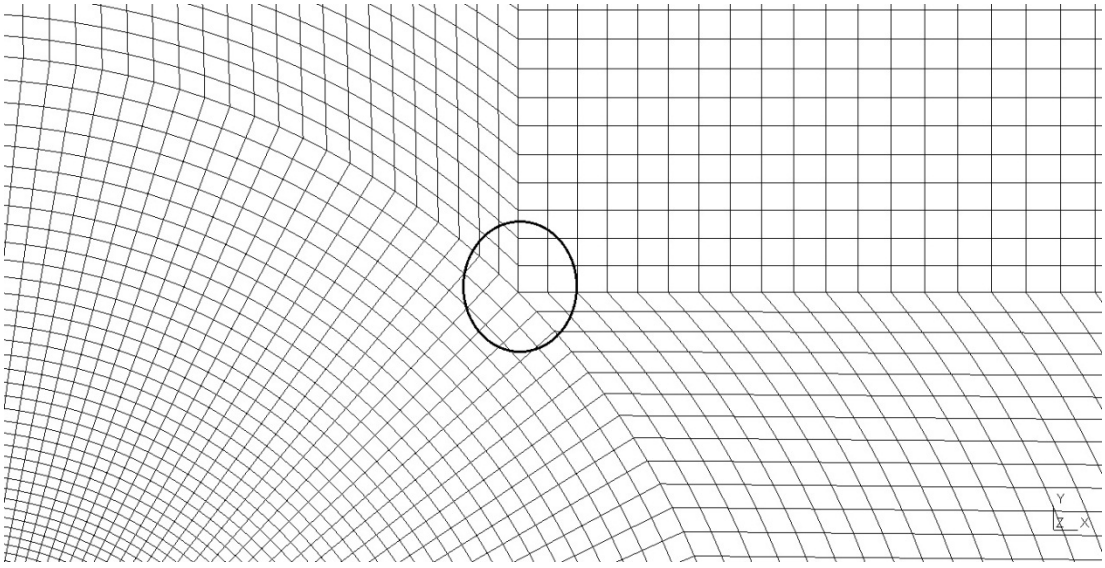

Figure 8: Closer view to the mesh

Likewise physical dimensions of the domain, the mesh topology is similar to that of reference [12]. There are 120 points in the circular region around the cylinder with a stretching factor of 1.032, stretching radially outwards. In the wake centerline, half

of cross-stream direction, and on the circumference of the cylinder there are 185 (120 + 65), 153 (120 + 33), and 192 points, respectively. At the inflow region there are 20 points on the centerline. Finally, there are 21 points in the spanwise direction.

In the literature, several types of meshes have been used such as, O- , C- (see Figure 9). However, for these mesh types, the inlet region is far away from the cylinder where unnecessarily large number of grids is located. In the present mesh, in the inlet region the grid resolution is satisfactory. However, the wake region needs more grids since the flow structure is turbulent there.

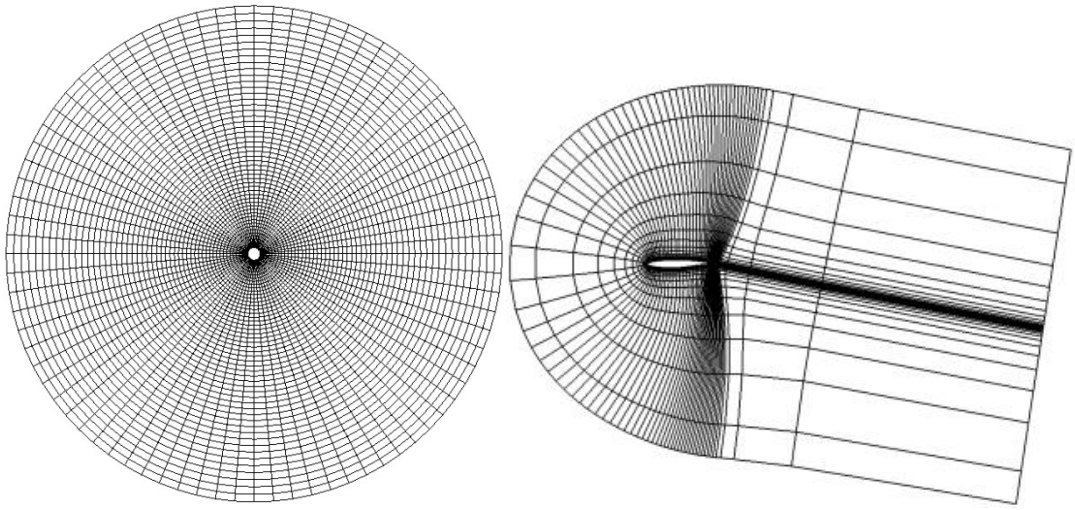

Figure 9: (left): O-mesh; (right): C-mesh [39].

As seen from Table 3, the number of layers in spanwise direction is lower than that of some resources. Also, as other resources, 32 layers case was tested as well but this case gave worse results, possibly due to increased anisotropy of the meshes. So, it is concluded that in order to use 32 layers, the mesh resolution in streamwise and cross-stream directions should be increased. Using several amounts of layers in spanwise direction is a necessity because this type of flow is strictly 3D especially in the near

wake region due to vortex shedding mechanism and if a 2D simulation was conducted, the recirculation in the near-wake region would not be resolved. This can be observed by examining the streamwise velocity component along wake centerline of reference [8]. Since spanwise resolution is coarser than that of other resources, the total number of cells is lower.

The normal distance from cylinder surface to the first adjacent cell is $\Delta n = 4.8\text{x}10^{-3} D$ which is a little bit greater than that of other works. Note that, [9] took $\Delta n = 2.5\text{x}10^{-3} D$ which is considerably larger than others however, they utilized a different approach for which instead of refining the near wake, outside of the near-wall region is refined to obtain an excellent description of the coherent structures.

On the other hand, the non-dimensional distance from the wall surface, n^+, which is defined in eq. (4.31), should be smaller than one in order to solve viscous boundary layer region accurately as stated in page 106 of reference [1].

Table 3: Mesh specifications from several resources

Resource	N_z	N_{total}	Δn (Dx10^{-3})
[8]	32/64	870k/1.1m/1.7m	
[11]	32/48	870k/1.3m	2.5
[10]	48	500k/1.3m/2.4m	
[9]	48	10.8m/43.3m	210
[6]	32	1.2m	2.5
[7]	256	13m	
[12]	32	1.1m	3.5
Present	20	680k	4.8

As mentioned before, domain decomposition technique is employed so, the mesh is partitioned by GMSH [40] with METIS algorithm ([41]) although Chaco algorithm ([42]) produces the desired output as well. The type of partitioning is element-based

so, the interfaces are shared among the partitions and this is suitable for a FV application.

4.5.3. Case 2: $Re_D = 100$

For this case, the length of left, top, and bottom sides is 5*D*. The mesh which is shown in Figure 10 is coarser and there are nearly 17000 cells. Since the flow is 2D, there is only one layer in the spanwise direction. The distance from the adjacent cell to the cylinder is 1.6×10^{-2}.

At the left, top, and bottom boundaries velocity inlet BC is specified with u = 1 m/s and v = w = 0. At the right boundary, the BC is the same as in the Re = 3900 case. At the lateral sides symmetry BC is specified because the flow is 2D.

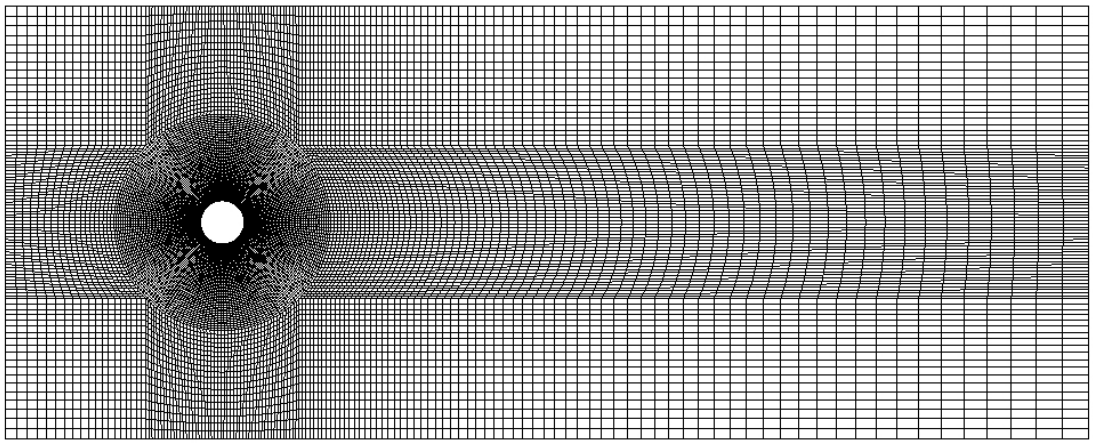

Figure 10: Mesh for Re = 100

4.6. Treatment of Boundary Conditions

At a boundary, eq. (4.63) is written as:

$$a_P \overline{v}_{i,P} = \sum_{\substack{N=\mathrm{nb}(P) \\ N \neq b}} a_N \overline{v}_{i,N} + s_i + a_b \overline{v}_{i,b} \tag{4.66}$$

The last term of eq. (4.66) will be determined according to one of the two basic boundary conditions: Dirichlet and Neumann. All specified boundary conditions are subsets of one of these BCs.

4.6.1. Dirichlet Boundary Conditions

For this type, the last term of eq. (4.66) is known hence, it will be included into the source term as:

$$s_i = s_i + a_b \overline{v}_{i,b} \tag{4.67}$$

Velocity inlet, periodic, and pressure outlet boundary conditions are of this kind of boundary condition. Firstly, for velocity inlet boundary condition, velocities at the boundary are given. For periodic boundary condition, the variables at the boundaries take their values from internal elements or cells. For pressure outlet the velocities at the boundary are found from the mass flow rate at the boundary. As a result, boundary variables are known explicitly for a Dirichlet boundary condition. Below, these boundary conditions will be examined in detail.

4.6.1.1. Periodic Boundary Condition

In all works on flow over circular cylinder, the spanwise length of the domain is πD which is considered to be the period in spanwise direction.

For periodic boundary condition, referring to Figure 11, the bold rectangle indicates the solution domain. The cells which are at the outside of the domain are imaginary cells and their values are the same as their periodic counterparts which are shown by

the same color. As a result, boundaries which are of periodic type will be treated as an internal face.

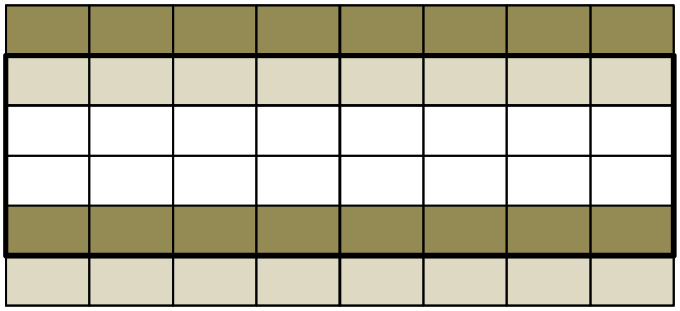

Figure 11: Periodic BC

4.6.1.2. Pressure Outlet Boundary Condition

A comment on this boundary condition is given in page 1198 of reference [12]:

> This boundary condition is known to be reflective [43]. When an inhomogeneous pressure distribution like the one in the large Kármán vortices is convected across the outflow boundary, small pressure disturbances are reflected back into the computational domain, travelling towards the inflow boundary where they are reflected back into the computational domain. An instantaneous distribution of the pressure and of the solution variables does not show any visible reflections, these have been considered as small. But it should be kept in mind, that this boundary condition imposes disturbances on the approaching flow which are purely numerical.

The reason of using this boundary condition instead of convective boundary condition which is used by [6, 8, 9, 11], is not based on physical arguments.

For the pressure outlet boundary condition, the static pressure at the boundary is set to zero so that all pressures are relative to outlet pressure. Since pressure is known at the boundary, mass flow rate can be calculated and subsequently, velocity at the boundary can be obtained. Note that, for both momentum and pressure correction equations, pressure outlet is of Dirichlet BC type. Considering eq. (A.13),

$$\begin{aligned}
&\bar{\mathbf{D}}_f = \mathbf{D}_P \\
&\left(\overline{\nabla p}\right)_f = \left(\nabla p\right)_b \\
&\mathbf{A}_f = \mathbf{A}_b \\
&\bar{\mathbf{v}}_f = \mathbf{v}_b \\
&\mathbf{NN}' = 0 \\
&p_N = p_b
\end{aligned} \tag{4.68}$$

So eq. (A.13) becomes:

$$\dot{m}_f = \rho \mathbf{v}_b \cdot \mathbf{A}_b + \rho \mathbf{D}_P \left(\nabla p\right)_b \cdot \mathbf{A}_b - a_N^{\mathrm{pc}} \left(p_N - p_P\right) + a_N^{\mathrm{pc}} \left(\nabla p_P \cdot \mathbf{PP}'\right) \tag{4.69}$$

where, in the calculation of a_N^{pc}, the only difference is that $\mathbf{D}_f$ is used instead of $\mathbf{D}_P$.

4.6.2. Neumann Boundary Condition

For Neumann boundary condition, the boundary values are not known explicitly but they can be obtained using other given relations such as the given diffusive flux at the boundary. Top and bottom boundaries are of symmetry boundary condition, which is explained in detail below, is a kind of Neumann boundary condition.

4.6.2.1. Symmetry Boundary Condition

This boundary condition is also used by [7] and is also referred as slip side wall boundary condition for which there is no shear stress which is also used by [18] as cited in [12]. Alternative boundary condition is the periodic boundary condition which is used by [9] and [44]. Additionally, on these boundaries, farfield BC for which tangential velocity is set free-stream velocity, can be used as [12] although [15] as cited in [12] stated that the use of farfield BC at y/D = ±10 (which is the case in this work as well), which is the case in this work as well, causes an acceleration of the flow at the edge of the wake region.

Since the gradient of normal velocity at the boundary is zero for symmetry BC, diffusive flux will also be zero as shown below.

$$\begin{aligned} J_b^{\text{diff}} &= \left(\mu_{\text{eff}} \frac{\partial \overline{v}_i}{\partial x_j} A_j \right)_b = a_b^{\text{diff}} \left(\overline{v}_{i,b} - \overline{v}_{i,P} \right) + s_i^{\text{cd}} = 0 \\ \Rightarrow a_b^{\text{diff}} \overline{v}_{i,b} &= a_b^{\text{diff}} \overline{v}_{i,P} - s_i^{\text{cd}} \end{aligned} \tag{4.70}$$

Substituting the result of the equation above into eq. (4.66) yields:

$$a_P \overline{v}_{i,P} = \sum_{\substack{N=\text{nb}(P) \\ N \neq b}} a_N \overline{v}_{i,N} + s_i + a_b^{\text{diff}} \overline{v}_{i,P} - s_i^{\text{cd}} \tag{4.71}$$

As a result,

$$\begin{aligned} a_P &= a_P - a_b^{\text{diff}} \\ s_i &= s_i - s_i^{\text{cd}} \end{aligned} \tag{4.72}$$

After solving $\overline{v}_i^P$, the boundary variable can be updated as,

$$\overline{v}_{i,b} = \overline{v}_{i,P} - \frac{s_i^{\text{cd}}}{a_b^{\text{diff}}} \tag{4.73}$$

Chapter 5

RESULTS AND DISCUSSIONS

5.1. Introduction

To validate the self-made code, which is able to solve Navier-Stokes equation on unstructured grids with parallelization, two cases were considered. In the first case, for which Re_D = 100, the flow is laminar (no turbulence model implemented), unsteady and periodic. Whereas in the second case, for which Re_D = 3900, the flow is turbulent which is initiated in the shear layers and since the flow is turbulent, it is inevitably unsteady.

For Re_D = 100 case, regarding mean variables, mean drag coefficient (with drag coefficient history), mean back-pressure coefficient (with pressure coefficient history), Strouhal number which is obtained by estimating the period of lift coefficient, mean velocity field, and mean recirculation length were investigated.

Considering instantaneous variables at Re_D = 100, instantaneous pressure field and instantaneous stream function during a vortex shedding cycle were investigated.

For Re_D = 3900 case, in addition to the mean variables found in Re_D = 100, mean friction coefficient, mean streamwise velocity together with its minimum value along wake centerline, separation angle, and turbulence statistics such as mean streamwise and shear stresses were calculated.

5.2. Case 1: $Re_D = 100$

In this case, the flow is laminar, unsteady and periodic. Note that, since the flow is laminar, no turbulence model implemented for this case.

Drag coefficient, C_d, lift coefficient, C_l, and pressure coefficient, C_p can be calculated with the following equations.

$$C_{\mathrm{d}} = \frac{F_x}{p_{\mathrm{dyn}}} \qquad C_{\mathrm{l}} = \frac{F_y}{p_{\mathrm{dyn}}} \qquad C_{\mathrm{p}} = \frac{p - p_\infty}{p_{\mathrm{dyn}}} \tag{5.1}$$

where, F_x and F_y are the streamwise and cross-stream force components, respectively, p_∞ is the free-stream or static pressure which is taken as zero, and p_{dyn} is the dynamic pressure as:

$$p_{\mathrm{dyn}} = \frac{1}{2}\rho U_\infty^2 A_{\mathrm{p}} \tag{5.2}$$

For Re_D = 100 case, the free stream velocity is $U_\infty = 1$ m/s and A_{p} is the planform area of the cylinder which is πD.

Mean drag coefficient is found as 1.47 which is the same as the value found by [13]. Also the history of drag coefficient is shown in Figure 12 from which it is clear that, starting averaging at 150$^{\mathrm{th}}$ second is a good choice because the initial transients die out before 150$^{\mathrm{th}}$ second.

Without using power spectrum density, Strouhal number which is defined in eq. (5.3) can be obtained by measuring the period, τ_p which is nearly 6 seconds as shown in Figure 13. For Re = 100 case, the lift coefficient is periodic and there is only one

dominant frequency (period) as opposed to Re = 3900 case for which power spectrum density should be calculated in order to calculate dominant frequency. The Strouhal number is nearly 0.17 which is nearly the same as 0.16 which is found by [13].

$$St = \frac{fD}{U_\infty} = \frac{D}{\tau_p U_\infty} \tag{5.3}$$

Von Kármán's street can be observed in Figure 14 in which contour plot of instantaneous pressure field is shown at the end of the simulation (200^{th} second) which is just an arbitrary time aimed to show the instantaneous pressure field. To show the vortex street better a complete vortex shedding cycle is presented in Figure 15. On the other hand, mean flow field is presented in Figure 16 from which the recirculation length is nearly 2 X/D.

Pressure coefficient along the cylinder surface is shown in Figure 17. Reference [13] gives the back-pressure coefficient which is the pressure coefficient at the $\theta = 180°$ as -0.71 which is exactly the same as the present result as evident from the figure.

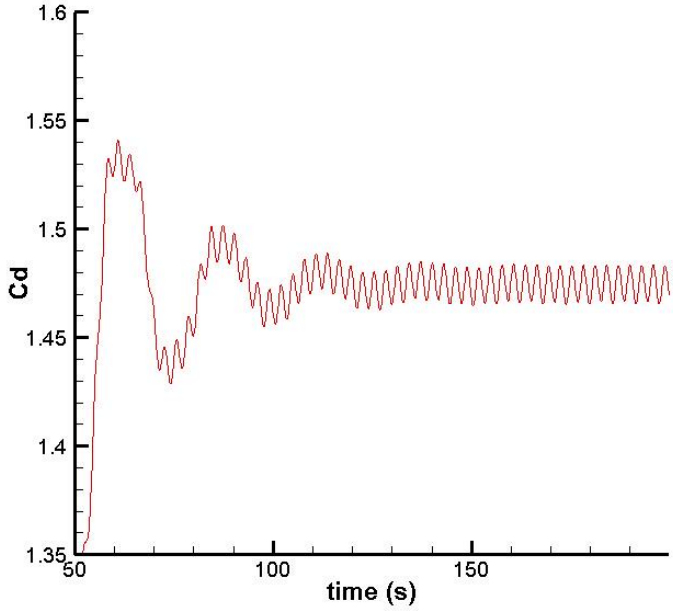

Figure 12: Drag history at $Re_D = 100$.

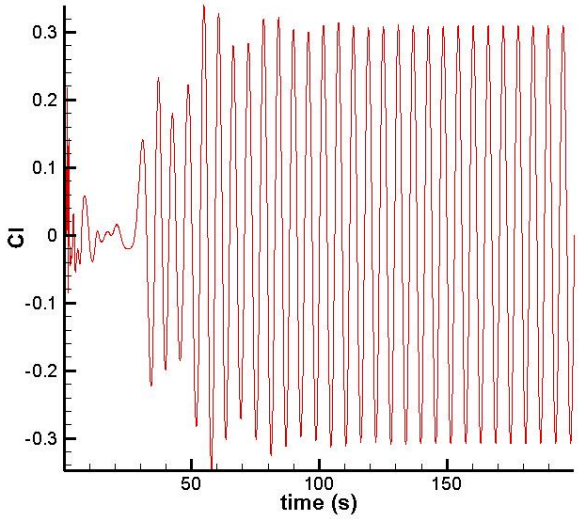

Figure 13: Lift history at $Re_D = 100$.

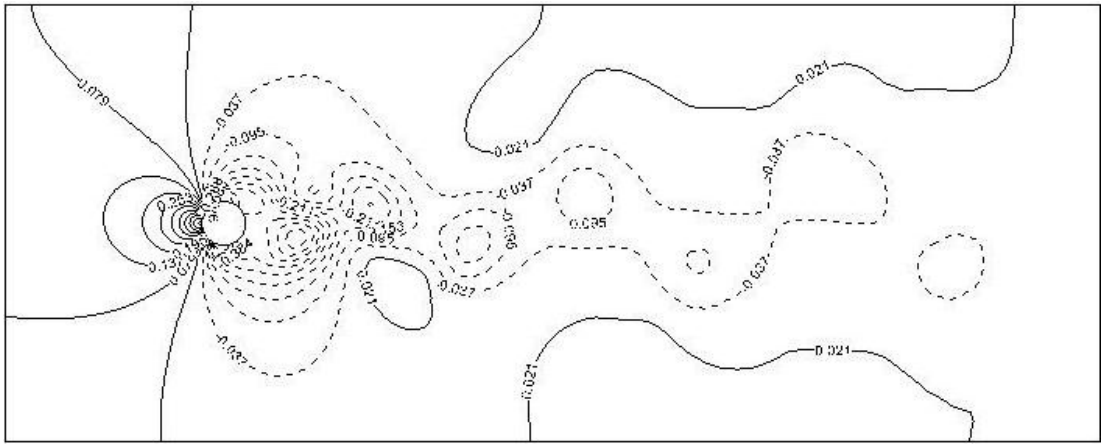

Figure 14: Instantaneous contour plot of pressure (Pa) field at $Re_D = 100$. Dashed lines denote negative values of pressure.

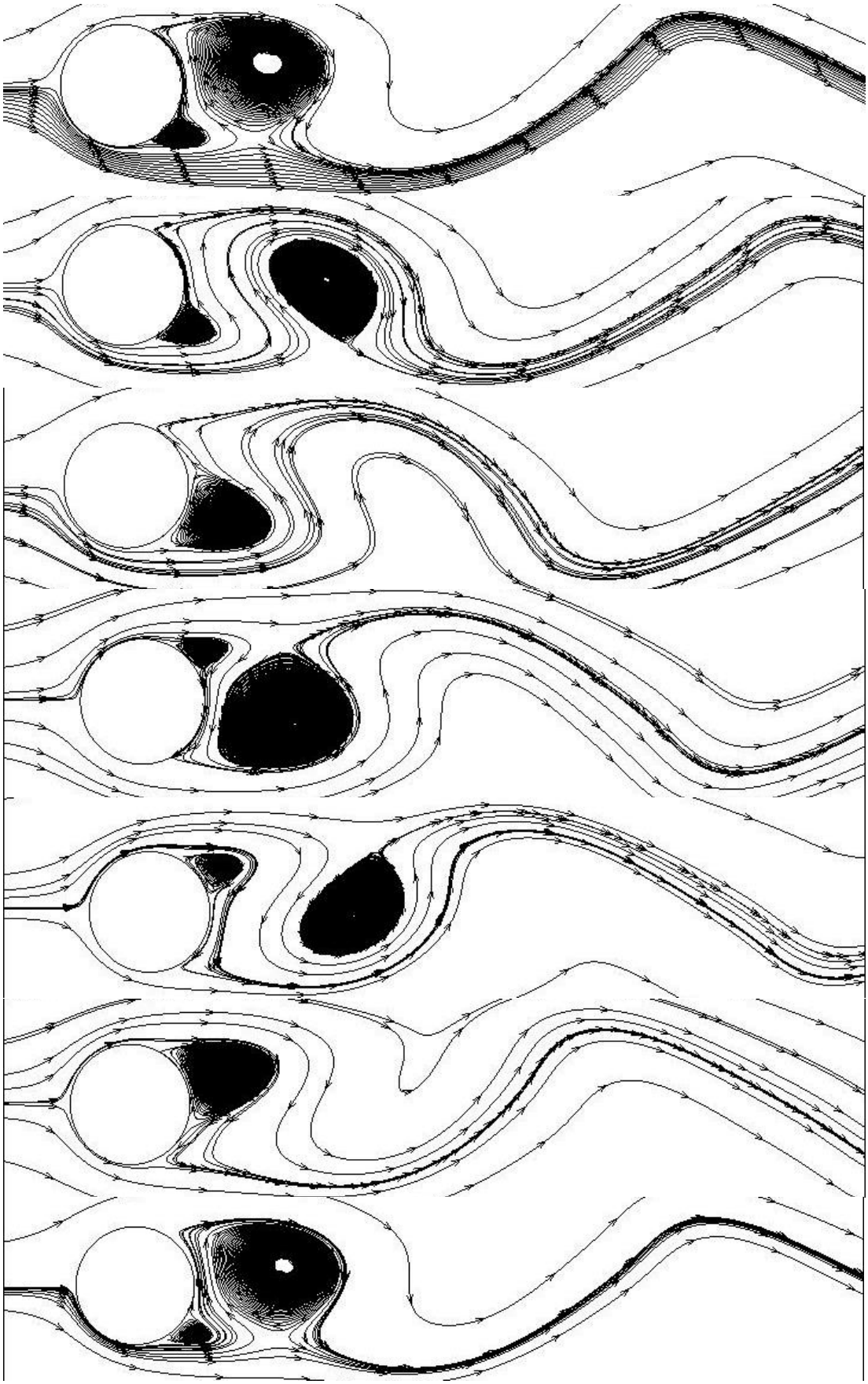

Figure 15: Stream function at Re_D = 100. From top to bottom at t = 190, 191, 192, 193, 194, 195, 196 seconds.

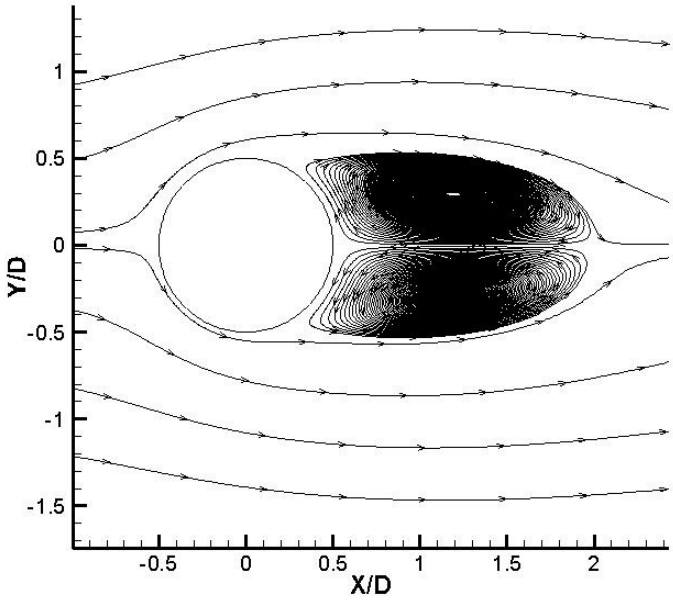

Figure 16: Mean flow field at $Re_D = 100$.

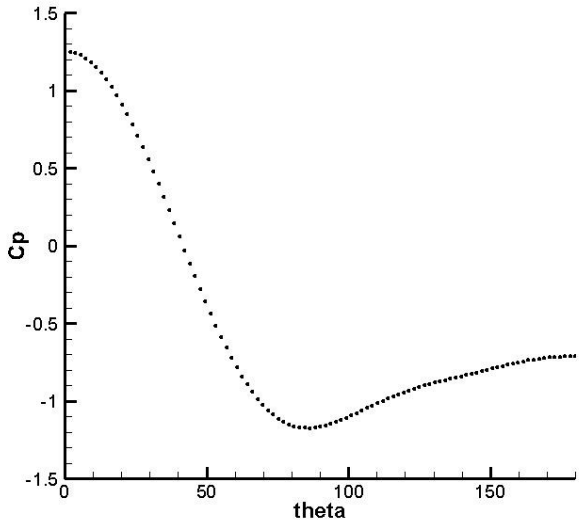

Figure 17: Pressure coefficient at $Re_D = 100$.

5.3. Case 2: $Re_D = 3900$

In this case, the flow is turbulent in the wake region but the initiation of turbulence starts at shear layers.

Mean streamwise velocity along the centerline of the wake is shown in Figure 18. It is obvious that the minimum velocity is greater than that of the experimental data. Additionally, the difference becomes much more distinguishable away from the cylinder. In fact, a possible explanation is given by reference [7] which is reproduced in Figure 19, maximum n^+ or Y^+ , which is the normal distance to the cylinder surface and defined in eq. (4.31)-, is 3.4 and occurs for case 4 (see Table 4) and as a result of the rather high value of n^+ the minimum velocity and the point of turnover is different than other cases. Note that the mean streamwise velocity in the wake centerline in Figure 19 is nearly the same as the present result as shown in Figure 18. Additionally, in Table 4, for case 4, spanwise length is as twice as that of cases 1, 2, and 3 but at the same time, number of layers in spanwise direction is also double of that of the same cases. Moreover, for case 4, SGS model is dynamic model as the other cases except case 2 which used Smagorinsky model which is the model used in this work. As a result, it can be concluded that n^+ has a strong effect on the accuracy of the results. For the present work, the maximum of temporal mean value of n^+ is 4.6 which is higher than the value (3.4) for case 4. Hence, it can be concluded that, the normal distance between the cylinder surface and closest cells to the cylinder surface should be smaller. An immediate solution which is to increase the resolution in streamwise and cross-stream directions only would not work because the spanwise resolution should be increased accordingly in that case. Similarly, the opposite action that is, increasing spanwise resolution while keeping others the same, would not

work. As a result, not only in a specific direction but in all directions grid resolution should be increased.

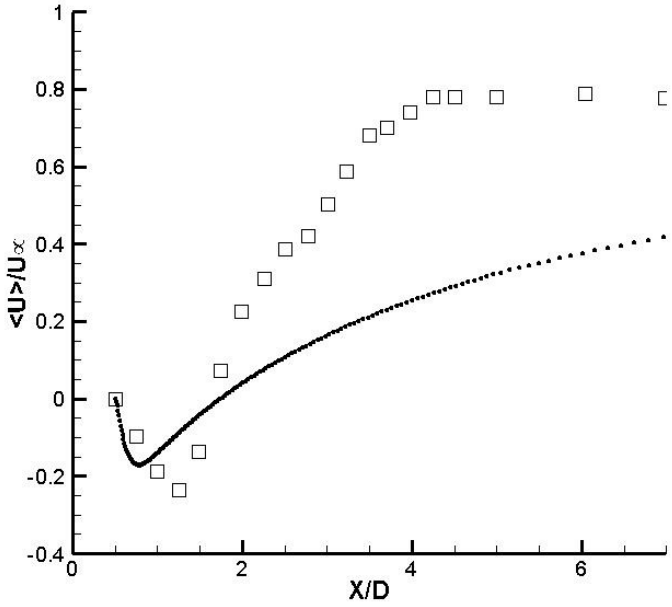

Figure 18: Mean streamwise velocity along the wake centerline at Re_D = 3900. Points denote present result; squares denote the combination of experimental data of [5] and [4].

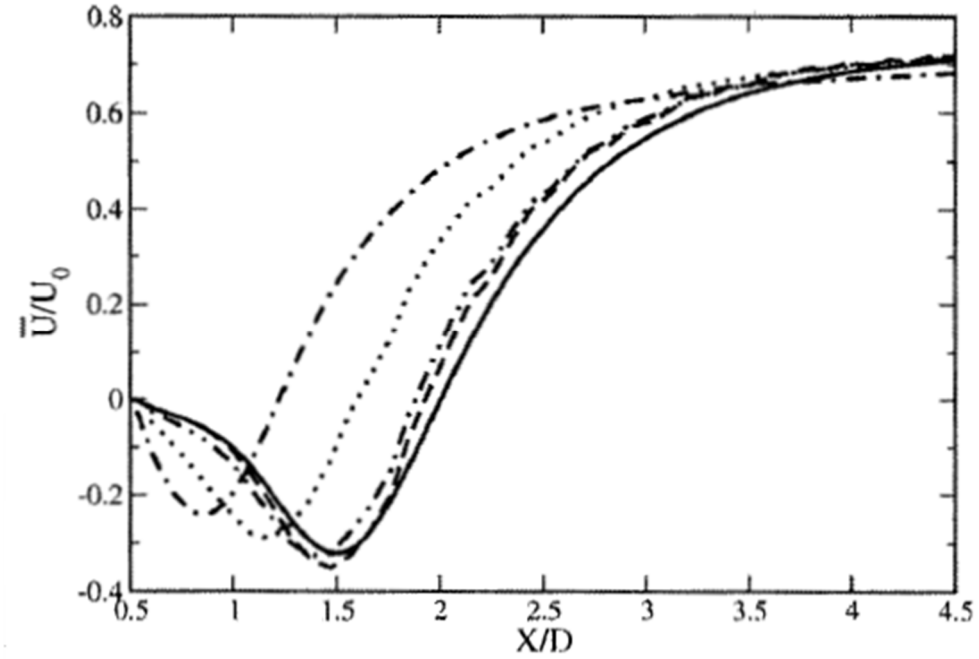

Figure 19: Sensitivity study for the mean streamwise velocity along the wake centerline (Y/D = 0) for a single cylinder at $Re_{D,Uo}$ = 3900, — case 1; ···, case 2; — — case 3; — · —, case 4; and ·· — ··, case 5. [7]

Table 4: Description of different cases used for sensitivity study [7][1].

Case	*Lz*	*LzNz*	Y^+	Model (Blending)
1	4D	256	1.7	Dyn (99% CDS +1% UP)
2	4D	256	1.7	No model (99% CDS +1% UP)
3	4D	256	1.7	Dyn (pure CDS)
4	8D	512	3.4	Dyn (99% CDS +1% UP)
5	8D	512	1.7	Dyn (99% CDS +1% UP)

Mean streamwise velocity at *X*/*D*=1.06 is shown in Figure 20. There is a very good agreement with the DNS results of [18] however; the same evaluation cannot be made for the mean cross-stream velocity. Although the trend is the same, the cross-stream velocity is more oscillatory than the present result. However, the difference in the order of magnitudes is not very much. This difference is due to relatively course grid resolution as compared with other references in Table 3.

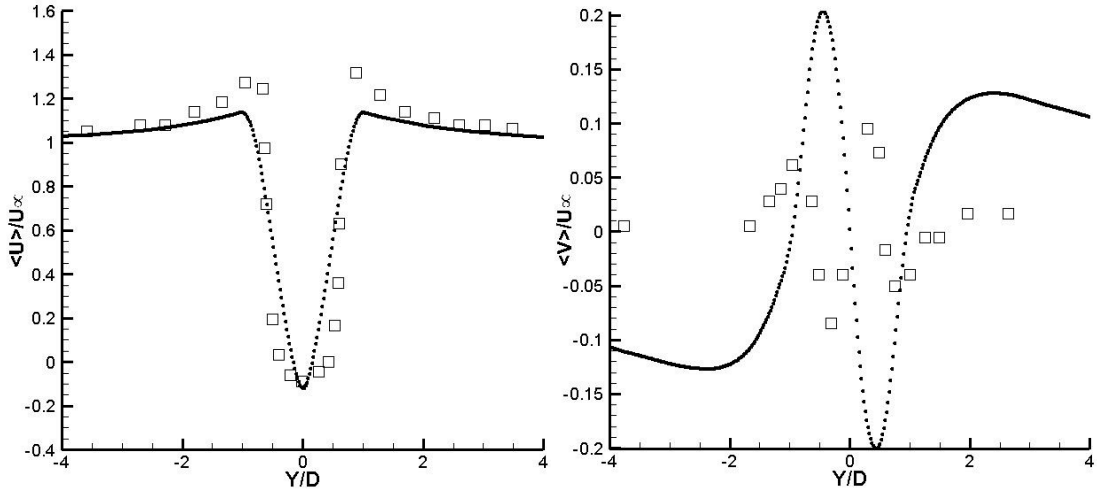

Figure 20: (left): Mean streamwise velocity at X/D=1.06 at Re_D = 3900. Squares denote DNS results of [18]; (right): Mean cross-stream velocity at X/D=1.06. Squares denote DNS results of [18].

[1] *Lz*: Spanwise length
LzNz: Number of layers in spanwise direction
Y^+: Corresponds to max(n^+)
Dyn: Dynamic
UP: Upwind
CDS: Central difference scheme

In addition to drag coefficient, C_d, lift coefficient, C_l, and pressure coefficient, C_p, also friction coefficient, C_f can be calculated with the following equation.

$$C_f = \frac{\tau_w}{p_{dyn}} \tag{5.4}$$

where, τ_w is the wall shear stress, and p_{dyn} is defined in eq. (5.2).

Note that, free stream velocity is $U_\infty = 3.9$ m/s. The instantaneous variables are first, averaged in spanwise direction and then in time for the last 15 seconds. The averaged quantities are shown in Table 5 together with results from several quantities. As expected, the mean drag coefficient is less than that of other works (see Table 5) because of lower SGS constant (0.065) while it is either 0.1 for all other works or the model is dynamic model so that the SGS constant is not a constant anymore. The reason is that, increasing SGS constant prevents residuals to drop below the imposed criterion which is $5\text{x}10^{-5}$ using only 10 inner iterations per time step and using higher number of iterations increases the simulation time. History of drag coefficient is shown in Figure 21 in which the initial transients die out after about 25 seconds. So, the averaging of the variables is started after 25 seconds.

Table 5: Mean quantities from several resources and present work

Resources	$\langle C_d \rangle$	St	L_R/D	$\langle C_{pb} \rangle$	θ_{sep}	U_{min}/U_∞
[8]	1.099	0.2	1.115	-1.049	87.9	
[11]	1.08	0.216	1.09	-1.03	88.1	
[10]	1.04	0.210	1.35	-0.94	88.0	-0.37
[9]		0.208	1.56			-0.26
[6]	1.00	0.218	1.35		87.6	-0.31
[7]	1.02	0.207	1.49	-0.93	86	-0.32
[12]	0.978	0.209	1.64	-0.85	88.2	
[5] (Exp)[2]	0.98±0.05	0.215±0.005	1.33±0.2	-0.9±0.05	85±2	-0.24±0.1
Present	0.82	0.06	1.6	-1.6	86	-0.17

[2] This is an experimental data and cited in [7].

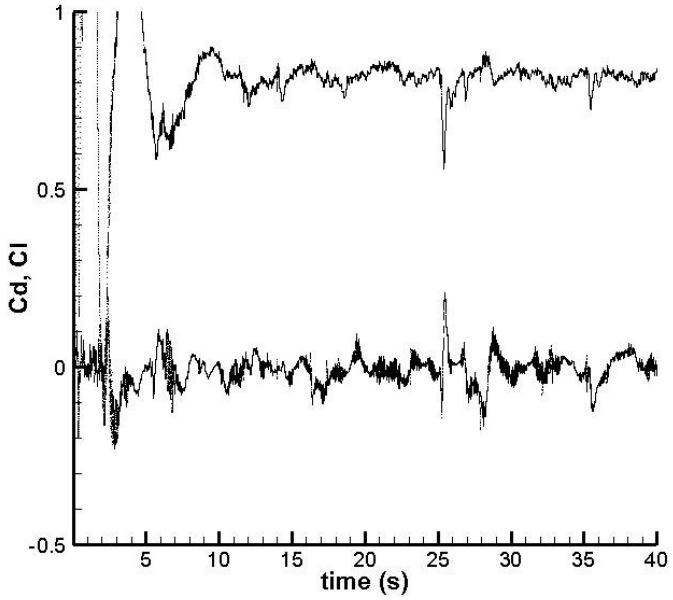

Figure 21: History of drag and lift coefficients at Re_D = 3900. (top): drag coefficient; (bottom): lift coefficient.

The recirculation length is 1.6 which is in the range of the other values in Table 5. The length of the recirculation zone (see Figure 22) is closely related to the mean drag coefficient in a way that in that zone there are two counter-rotating vortices and the velocity in the center is in opposite direction of the main stream. So, the longer the recirculation zone, greater the mean drag coefficient. Accordingly, the back pressure coefficient which is the pressure at the back of the cylinder is greater in this work, causing mean drag coefficient to decrease. The value of back pressure can be spotted in Figure 23. Note that, initially, when θ is small ($\theta < 50°$) the values are matching with the reference values but then for $\theta > 50°$ C_p diverges from DNS results. The same is valid for friction coefficient (see Figure 23) as well. This is because the grid resolution in the near wake is finer than that of in the far wake region. Hence, the grid resolution in the far wake region should be increased.

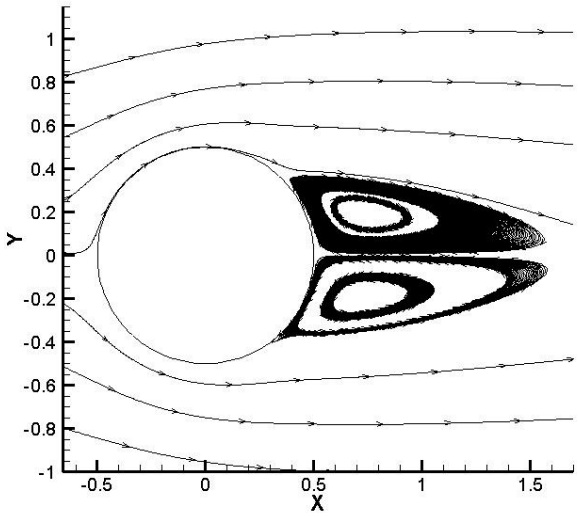

Figure 22: Mean flow field in recirculation zone at $Re_D = 3900$.

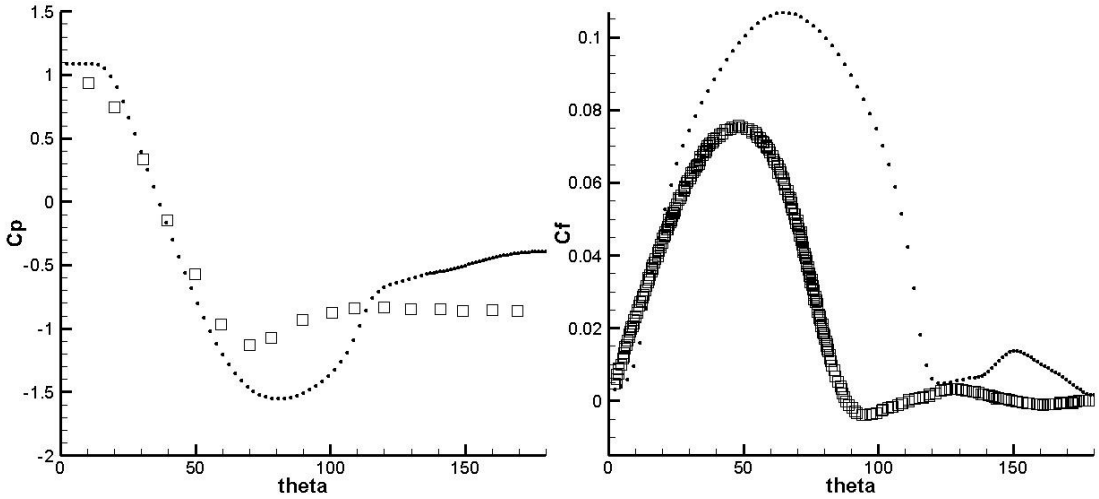

Figure 23: (left): Pressure coefficient at $Re_D = 3900$. Squares denote DNS results of [18]; (right): Friction coefficient. Squares denote LES results of [8]. Points denote present results.

Turbulence statistics have also been tested. In Figure 24, mean streamwise stress in shown. It is found that although the pattern of the present result resembles the reference data as shown in Figure 24, there is an order of magnitude difference between two data. Additionally, the present result was not able to capture a symmetric pattern. This is due to the coarse grid resolution.

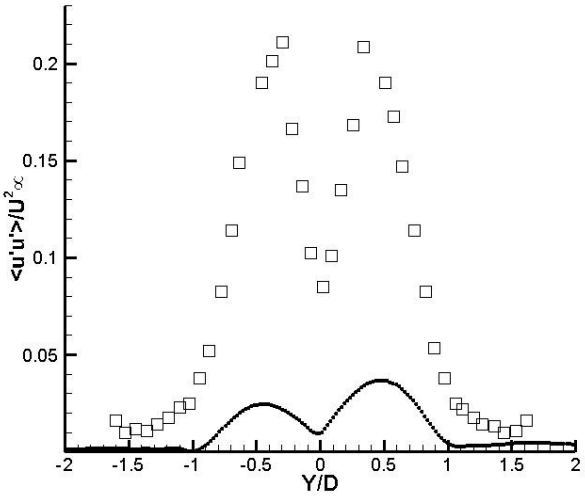

Figure 24: Mean streamwise stress at Re_D = 3900. Solid line denotes present result; squares denote LES results of [9].

In contrary to mean streamwise stress, mean shear stress has the same order of magnitudes with the reference data (see Figure 25). Yet, the reference data is more oscillatory than the present result.

From power spectrum density of both lift force and u-velocity taken at X/D = 2 (see Figure 26), Strouhal number (eq. (5.3)), which is defined below, is found as 0.06 which is lower than other values in Table 5. The value of Strouhal number is consistent with the results of turbulence statistics because relatively low Strouhal number means that oscillations around the cylinder have a lower frequency. Hence turbulence statistics which are related to turbulent oscillations have been found to be lower than the reference values as was shown in Figure 24 and Figure 25.

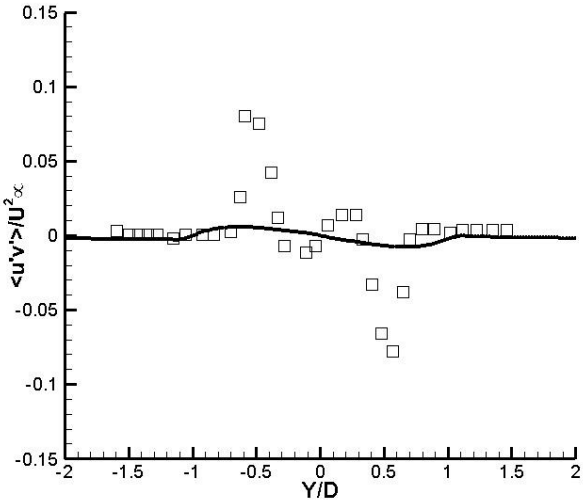

Figure 25: Mean shear stress at Re_D = 3900. Solid line denotes present result; squares denote LES results of [9].

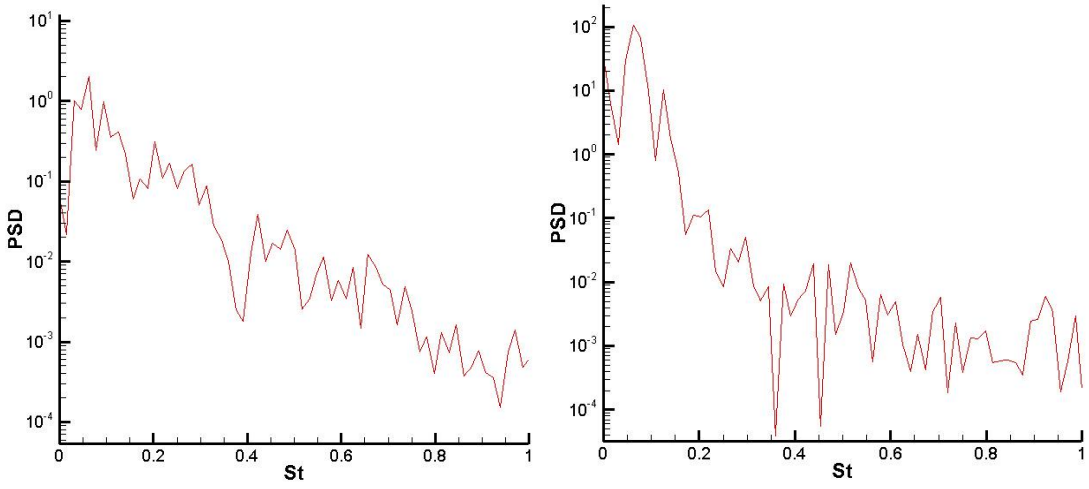

Figure 26: Power spectrum density of the (left): lift force; (right): streamwise velocity at X/D = 2 at Re_D = 3900.

The simulation is completed in approximately 12 hours using a time step of 0.001 seconds, with nearly 680000 grids, and 20 layers in spanwise direction. When the layers in spanwise direction is increased from 20 to 32, it takes about 18 hours.

Chapter 6

CONCLUSIONS

In this work, a computer code was developed to solve turbulent flow equations on unstructured grids using Large Eddy Simulation (LES) with Smagorinsky model as the sub-grid scale model, in C++ language.

To validate the self-made computer code, which is able to solve LES Navier-Stokes equation on unstructured grids, a flow past a circular cylinder at two cases were considered. In the first case, a laminar and periodic flow at $Re_D = 100$, while in the second case, a turbulent flow at $Re_D = 3900$ was analyzed.

For $Re_D = 100$, all the results were found to be accurate when compared with the reference [13]. Mean variables such as mean drag coefficient, Strouhal number, and mean back-pressure coefficient are found to be well matching with the reference data. Instantaneous pressure field and a complete vortex shedding cycle were also presented in order to show that the vortex shedding mechanism was captured as well. From the mean flow field, recirculation length was also estimated accurately. As a result, it was validated that for a laminar and periodic flow past a circular cylinder at $Re_D = 100$ was accurately simulated.

In the second case in which the flow was turbulent, a LES was carried out. The turbulence model was Smagorinsky model with $C_{SGS} = 0.065$. Mean drag coefficient

was found to be close to that of the experimental data. In order to obtain Strouhal number, power spectrum density is calculated and accordingly Strouhal number was found to be a little bit lower and this relatively small Strouhal number showed that the turbulence oscillations in the present work were lower than that of the references. As a support, turbulence statistics such as mean streamwise stress and mean shear stress were found to be rather lower than that of references. Mean pressure coefficient and mean friction coefficient around the cylinder surface showed that at the upstream of the cylinder ($\theta < 30$), the coefficients are in agreement with the reference values. However, due to relatively coarse grid resolution at the downstream of the cylinder, the mean pressure coefficient and the mean friction coefficient diverged from the reference values. Besides the coarse grid resolution at the wake region, generally the grid resolution of the whole domain was not fine enough due to insufficient computing resources. As a comparison, in reference [7], 21 million cells was used for the LES of $Re_D = 3900$, while in this work 680000 cells are used. Additionally, from the mean pressure coefficient data, back-pressure coefficient was obtained and it was found that it is higher than the reference data. The value of back-pressure coefficient was consistent with the value of mean drag coefficient because relatively high negative back-pressure coefficient resulted in a lower value of the mean drag coefficient.

REFERENCES

[1] H. K. Versteeg and W. Malalasekera, An Introduction to Computational Fluid Dynamics, 2. ed., Pearson, 2007.

[2] M. M. Rahman, M. M. Karim ve M. A. Alim, «Numerical investigation of unsteady flow past a circular cylinder using 2-D finite volume method,» *Journal of Naval Architecture and Marine Engineering,* 2007.

[3] C. Norberg, "An experimental investigation of the flow around a circular cylinder: Influence of aspect ratio," *Journal of Fluid Mechanics,* vol. 258, pp. 287--316, 1994.

[4] L. Ong and J. Wallace, "The velocity field of the turbulent very near wake of a circular cylinder," *Experiments in Fluids,* vol. 20, no. 6, pp. 411-453, 1996.

[5] L. M. Lourenco and C. Shih, *Characteristics of the plane turbulent near wake of a circular cylinder, a particle image velocimetry study,* Published in Beaudan and Moin (1994), data taken from Kravchenko and Moin (2000), 1993.

[6] K. Mahesh, G. Constantinescu and P. Moin, "A numerical method for large-eddy simulation in complex geometries," *Journal of Computational Physics,* vol. 197, pp. 215-240, 2004.

[7] I. Afgan, Y. Kahil, S. Benhamadouche and P. Sagaut, "Large eddy simulation of the flow around single and two side-by-side cylinders at subcritical Reynolds numbers," *Physics of Fluids,* vol. 23, no. 7, 2011.

[8] M. Breuer, "Large eddy simulation of the subcritical flow past a circular cylinder: Numerical and modeling aspects," *International Journal for Numerical*

Methods in Fluids, vol. 28, pp. 1281-1302, 1998.

[9] P. Parnaudeau, J. Carlier, D. Heitz and E. Lamballais, "Experimental and numerical studies of the flow over a circular cylinder ar Reynolds number 3900," *Physics of Fluids,* vol. 20, no. 8, 2008.

[10] A. G. Kravchenko ve P. Moin, «Numerical studies of flow over circular cylinder at Re=3900,» *Physics of Fluids,* cilt 12, no. 2, 2000.

[11] J. Frohlich, W. Rodi, P. Kessler, S. Parpais, J. P. Bertoglio and D. Laurence, "Large eddy simulation of flow around circular cylinders on structured and unstructured grids," in *Notes on Numerical Fluid Mechanics*, vol. 66, Vieweg Verlag, Braunschweig, 1998, pp. 319-338.

[12] Franke, J. and Frank, W., "Large eddy simulation of the flow past a circular cylinder at Re=3900," *Journal of Wind Engineering and Industrial Aerodynamics,* pp. 1191-1206, 2002.

[13] Hoffman, J., "Efficient computation of mean drag for the subcritical flow past a circular cylinder using general Galerkin G2," *Internatinal journal for numerical methods in fluids,* 2000.

[14] Beaudan P. and Moin P., "Numerical experiments on the flow past a circular cylinder at sub-critical Reynolds number," Stanford University, 1994.

[15] Mittal, R., "Progress on LES of flow past a circular cylinder," *CTR Annual Reseach Briefs, Center for Turbulence Research, Stanford, CA 94305,* pp. 233-241, 1996.

[16] Liaw, K. F., *Simulation of flow around bluff bodies and bridge deck sections using CFD,* Nottingham: University of Nottingham, 2005.

[17] Lübcke, H., Schmidt, Sc., Rung, T. and Thiele, F., "Comparison of LES and

RANS in bluff-body flows," *Journal of Wind Engineering and Industrial Aerodynamics,* vol. 89, no. 14-15, pp. 1471-1485, 2001.

[18] Ma, X., Karamanos, G. S. and Karniadakis, G. E., "Dynamics and low-dimensionality of a turbulent wake," *Journal of Fluid Mechanics,* no. 410, pp. 29-65, 2000.

[19] L. F. Richardson, Weather Prediction by Numerical Process, Cambridge: Cambridge University Press, 1922.

[20] S. B. Pope, Turbulent Flows, Cambridge University Press, 2000.

[21] A. N. Kolmogorov, "The local structure of turbulence in incompressible viscous fluid for very large Reynolds numbers," *Dokl. Akad. Nauk SSSR 30,* pp. 299-303, 1941.

[22] B. M. Sumer and J. Fredsoe, "Hydrodynamics Around Cylindrical Structures," *Advanced Series on Ocean Engineering,* vol. 26, 2006.

[23] C. Wieselberger, "Neuere Feststellungen uber die Gesetze des Flussigkeits-und Luftwiderstands," *Phusics, Z,* vol. 22, p. 321, 1921.

[24] J. H. Ferziger and M. Peric, Computational Methods for Fluid Dynamics, 3. ed., Springer, 2002.

[25] I. Sezai, *Computational Fluid Dynamics, Lecture Notes,* Department of Mechanical Engineering, Eastern Mediterranean University, 2012.

[26] R. Peyret and E. Krause, *Advanced turbulent flow computations,* Vienna: Springer-Verlag, 2000.

[27] J. Smagorinsky, "General circulation experiments with the primitive equations, i. the basic experiment," *Monthly Weather Review,* vol. 91, pp. 99-164, 1963.

[28] J. Bardina, J. H. Ferziger ve W. C. Reynolds, «Improved subgrid-scale models

for large-eddy simulation,» *AIAA,* 1980.

[29] M. Germano, U. Piomelli, P. Moin and W. H. Cabot, "A dynamic sub-grid scale eddy viscosity model," *Physics of Fluids,* vol. A, no. 3, pp. 1760-1765, 1991.

[30] Piomelli, U., Ferziger, J. and Moin, P., "New approximate boundary conditions for large eddy simulations of wall bounded flow," *Physics of Fluids,* p. 1061, 1989.

[31] D. K. Lilly, "On the application of the eddy viscosity concept in the inertial sub-range of turbulence," NCAR, 1966.

[32] D. K. Lilly, "The representation of small-scale turbulence in numerical simulation experiments," 1967.

[33] R. S. Rogallo and P. Moin, "Numerical simulation of turbulent flows," *Ann. Rev. Fluid Mech.,* vol. 16, pp. 99-137, 1984.

[34] J. W. Deardorff, "A numerical study of three-dimensional turbulent channel flow at large Reynolds numbers," *Journal of Fluid Mechanics,* vol. 41, pp. 453-480, 1970.

[35] C. M. Rhie and W. Chow, "Numerical study of turbulent flow past an airfoil with trailing edge seperation," *AIAA Journal,* vol. 21, pp. 1525-1532, 1983.

[36] C. D. Perez-Segarra, C. Farre, J. Cadafalch and A. Oliva, "Analysis of different numerical schemes for the resolution of convection-diffusion equations using finite-volume methods on three-dimensional unstructured grids. Part I: Discretization schemes," *Numerical Heat Transfer, Part B: Fundamentals,* vol. 49, no. 4, pp. 333-350, 2006.

[37] Smith, T. M., Curtis, O. C. and Alfred, L. A., "SIERRA/Premo–A new general purpose compressible," in *AIAA 32nd Fluid Dynamics Conference*, St. Louis,

2002.

[38] "The openMP API specification for parallel programming," [Online]. Available: http://openmp.org/wp/. [Accessed 2012].

[39] "Making Sense of CFD Grid Types," [Online]. Available: http://www.innovative-cfd.com/cfd-grid.html.

[40] C. Geuzaine and J. F. Remacle, "Gmsh: a three-dimensional finite element mesh generator with built-in pre- and post-processing facilities," *International Journal for Numerical Methods in Engineering,* vol. 79, no. 11, pp. 1309-1331, 2009.

[41] G. Karypis, Karypis Lab, 2011. [Online]. Available: http://glaros.dtc.umn.edu/gkhome/metis/metis/overview/. [Accessed 2012].

[42] Hendrickson, B. and Leland, R., "The Chaco user's guide, version 2.0," SAND94-2692, Sandia National Laboratories, Albuquerque, NM, 1994.

[43] Poinsot, T. and Lele, S. K., "Boundary conditions for direct simulations of compressible viscous flows," *Journal of Computational Physics,* no. 101, pp. 104-129, 1992.

[44] Tremblay, F., Manhart, M. and Friedrich, R., "DNS of flow around a circular cylinder at a subcritical Reynolds number with cartesian grids," in *Proceedings of the Eighth European Turbulence Conference*, Barcelona, Spain, EUROMECH, CIMNE, 27-30 June, 2000.

[45] M. Van Dyke, An Album of Fluid Motion, 10 ed., Stanford: Parabolic Press, 1982.

APPENDICES

Appendix A: Momentum Interpolation Method (MIM) For Unstructured Grids

Rewriting eq. (4.63) as:

$$a_{i,P}v_{i,P} = \sum_{N=\mathrm{nb}(P)} a_{i,N}v_{i,N} + b_{i,P} - V\left(\nabla p\right)_{i,P} \tag{A.1}$$

where, b is the source term excluding pressure source.

The equation above can be written in another form such as:

$$v_i = H_{i,P} - V_P D_{i,P}\left(\nabla p\right)_P \tag{A.2}$$

where,

$$H_{i,P} = \frac{\sum_{N=\mathrm{nb}(P)} a_{i,N}v_{i,N} + b_{i,P}}{a_{i,P}} \qquad D_{i,P} = \frac{1}{a_{i,P}} \tag{A.3}$$

Similarly for a neighbour cell N,

$$v_i = H_{i,N} - V_N D_{i,N}\left(\nabla p\right)_N \tag{A.4}$$

And for the cell face,

$$v_i = H_{i,f} - V_f D_{i,f}\left(\nabla p\right)_f \tag{A.5}$$

$H_{i,f}$ can be interpolated as:

$$H_{i,f} \approx \bar{H}_{i,f} = \bar{v}_{i,f} + V_f D_{i,f}\left(\overline{\nabla p}\right)_f \tag{A.6}$$

where,

$$
\begin{aligned}
\overline{v}_{i,f} &= (1-\alpha)\, v_{i,P} + \alpha v_{i,N} \\
D_{i,f} &= (1-\alpha)\, D_{i,P} + \alpha D_{i,N} \\
V_f &= (1-\alpha) V_P + \alpha V_N \\
\left(\overline{\nabla p}\right)_f &= (1-\alpha)(\nabla p)_P + \alpha (\nabla p)_N
\end{aligned}
\tag{A.7}
$$

Substituting eq. (A.6) into eq. (A.5) yields:

$$
v_{i,f} = \overline{v}_{i,f} + V_f D_{i,f} \left[\left(\overline{\nabla p}\right)_f - (\nabla p)_f \right] \tag{A.8}
$$

Inserting eq. (A.8) into eq. (4.36), the mass flow rate becomes,

$$
\dot{m}_f = \rho \overline{v}_{i,f} \cdot A_{i,f} + \rho V_f D_{i,f} \left[\left(\overline{\nabla p}\right)_f - (\nabla p)_f \right] \cdot A_{i,f} \tag{A.9}
$$

Note that, the last term in eq. (A.9) acts as a higher-order correction to the first-order mass flow rate.

$(\nabla p)_f \cdot A_{i,f}$ can be discretized as implemented in eq. (4.55) as:

$$
\nabla p_f \cdot A_f = \underbrace{\frac{p_N - p_P}{|\mathbf{PN}|} A_f^{PN}}_{\text{orthogonal term}} + \underbrace{\frac{\nabla p_N \cdot \mathbf{NN'} - \nabla p_P \cdot \mathbf{PP'}}{|\mathbf{PN}|} A_f^{PN}}_{\text{non-orthogonal term}} \tag{A.10}
$$

Substituting the equation above into eq. (A.9),

$$
\begin{aligned}
\dot{m}_f = {} & \rho \overline{v}_{i,f} \cdot A_{i,f} + \rho V_f D_{i,f} \left(\overline{\nabla p}\right)_f \cdot A_{i,f} \\
& - \rho D_{i,f} \left(\frac{p_N - p_P}{|\mathbf{PN}|} A_f^{PN} + \frac{\nabla p_N \cdot \mathbf{NN'} - \nabla p_P \cdot \mathbf{PP'}}{|\mathbf{PN}|} A_f^{PN} \right)
\end{aligned}
\tag{A.11}
$$

Further simplification can be obtained with,

$$
\frac{A_f^{PN}}{|\mathbf{PN}|} = \frac{\mathbf{A}_f \cdot \mathbf{A}_f}{\mathbf{A}_f \cdot \mathbf{PN}} \tag{A.12}
$$

Eq. (A.11) becomes,

$$\dot{m}_f = \rho \overline{v}_{i,f} \cdot A_{i,f} + \rho V_f D_{i,f} \left(\overline{\nabla p} \right)_f \cdot A_{i,f} - a_N^{\mathrm{pc}} \left(p_N - p_P \right) - a_N^{\mathrm{pc}} \left(\nabla p_N \cdot \mathbf{NN}' - \nabla p_P \cdot \mathbf{PP}' \right) \tag{A.13}$$

where,

$$a_N^{\mathrm{pc}} = \frac{\rho \left(D_{i,f} \cdot A_{i,f} \right) \cdot A_{i,f}}{A_{i,f} \cdot \mathrm{PN}_i} \tag{A.14}$$

Appendix B: Derivation Of SIMPLE Algorithm For Unstructured Grids

Rewriting eq. (A.5) as:

$$v_i - H_{i,f} = -V_f D_{i,f} \left(\nabla p\right)_f \tag{B.1}$$

If p^{c} and $\mathbf{v}^{\mathrm{c}}$ be the corrections needed to correct the guessed velocity and pressure fields, respectively, then they can be decomposed such as:

$$v_i = v_i^* + v_i^{\mathrm{c}} \tag{B.2}$$

$$p = p^* + p^{\mathrm{c}} \tag{B.3}$$

For a guessed pressure field p^*, eq. (B.1) is written as:

$$v_i^* - H_{i,f} = -V_f D_{i,f} \left(\nabla p^*\right)_f \tag{B.4}$$

Subtracting the equation above from eq. (B.1) yields:

$$v_i^{\mathrm{c}} - H_{i,f} = -V_f D_{i,f} \left(\nabla p^{\mathrm{c}}\right)_f \tag{B.5}$$

For SIMPLE method, the second term on the LHS is neglected. Then,

$$\mathbf{v}_f^{\mathrm{c}} = -\mathbf{D}_f \nabla p_f^{\mathrm{c}} \tag{B.6}$$

Decomposing mass flow rate as:

$$\dot{m}_f = \dot{m}_f^* + \dot{m}_f^{\mathrm{c}} \tag{B.7}$$

Hence, continuity equation (eq. (4.36)) can be written as:

$$\sum_{f=1}^{\mathrm{n_f}} \left(\dot{m}_f^* + \dot{m}_f^{\mathrm{c}}\right) = 0 \tag{B.8}$$

where,

$$\dot{m}_f^{\mathrm{c}} = \rho \mathbf{v}_f^{\mathrm{c}} \mathbf{A}_f \tag{B.9}$$

Substituting $\mathbf{v}_f^{\mathrm{c}}$ in eq. (B.6) into eq. (B.9),

$$\dot{m}_f^{\mathrm{c}} = -\rho \left(\mathbf{D}_f \nabla p_f^{\mathrm{c}} \right) \cdot \mathbf{A}_f \tag{B.10}$$

$\nabla p_f^{\mathrm{c}} \cdot \mathbf{A}_f$ can be discretized as implemented in eq. (4.52),

$$\nabla p_f^{\mathrm{c}} \cdot A_f = \underbrace{\frac{p_N^{\mathrm{c}} - p_P^{\mathrm{c}}}{\left|\mathbf{PN}\right|} A_f^{PN}}_{\text{orthogonal term}} + \underbrace{\frac{\nabla p_N^{\mathrm{c}} \cdot \mathbf{NN}' - \nabla p_P^{\mathrm{c}} \cdot \mathbf{PP}'}{\left|\mathbf{PN}\right|} A_f^{PN}}_{\text{non-orthogonal term}} \tag{B.11}$$

Using eq. (A.12) for the equation above,

$$\nabla p_f^{\mathrm{c}} \cdot A_f = \frac{\mathbf{A}_f \cdot \mathbf{A}_f}{\mathbf{A}_f \cdot \mathbf{PN}} \left(p_N^{\mathrm{c}} - p_P^{\mathrm{c}} \right) + \frac{\mathbf{A}_f \cdot \mathbf{A}_f}{\mathbf{A}_f \cdot \mathbf{PN}} \left(\nabla p_N^{\mathrm{c}} \cdot \mathbf{NN}' - \nabla p_P^{\mathrm{c}} \cdot \mathbf{PP}' \right) \tag{B.12}$$

Substituting the equation above into eq. (B.10),

$$\begin{aligned} \dot{m}_f^{\mathrm{c}} = & \frac{\rho \left(\mathbf{D}_f \mathbf{A}_f \right) \cdot \mathbf{A}_f}{\mathbf{A}_f \cdot \mathbf{PN}} \left(p_N^{\mathrm{c}} - p_P^{\mathrm{c}} \right) \\ & + \frac{\rho \left(\mathbf{D}_f \mathbf{A}_f \right) \cdot \mathbf{A}_f}{\mathbf{A}_f \cdot \mathbf{PN}} \left(\nabla p_N^{\mathrm{c}} \cdot \mathbf{NN}' - \nabla p_P^{\mathrm{c}} \cdot \mathbf{PP}' \right) \end{aligned} \tag{B.13}$$

This equation can be simplified by using eq. (A.14) such as:

$$\dot{m}_f^{\mathrm{c}} = a_N^{\mathrm{pc}} \left(p_N^{\mathrm{c}} - p_{\mathrm{P}}^{\mathrm{c}} \right) + a_N^{\mathrm{pc}} \left(\nabla p_N^{\mathrm{c}} \cdot \mathbf{NN}' - \nabla p_P^{\mathrm{c}} \cdot \mathbf{PP}' \right) \tag{B.14}$$

Putting eq. (B.14) into eq. (B.10) yields:

$$\sum_{N=\mathrm{nb}(P)} a_N^{\mathrm{pc}} \left(p_N^{\mathrm{c}} - p_P^{\mathrm{c}} \right) = \sum_{f=1}^{\mathrm{n_f}} \dot{m}_f^{*} - \sum_{N=\mathrm{nb}(P)} a_N^{\mathrm{pc}} \left(\nabla p_N^{\mathrm{c}} \cdot \mathbf{NN}' - \nabla p_P^{\mathrm{c}} \cdot \mathbf{PP}' \right) \tag{B.15}$$

Thus, pressure correction equation can be written as:

$$a_P^{\mathrm{pc}} p_P^{\mathrm{c}} = \sum_{N=\mathrm{nb}(P)} \left(a_N^{\mathrm{pc}} p_N^{\mathrm{c}} + b_P^{\mathrm{pc}} \right) \tag{B.16}$$

where $a_{\mathrm{N}}^{\mathrm{pc}}$ is defined in eq. (A.14) and,

$$\begin{aligned} a_P^{\mathrm{pc}} &= \sum_{N=\mathrm{nb}(P)} a_N^{\mathrm{pc}} \\ b_P^{\mathrm{pc}} &= -\sum_{f=1}^{\mathrm{n_f}} \dot{m}_f^* + \sum_{N=\mathrm{nb}(P)} a_N^{\mathrm{pc}} \left(\nabla p_N^{\mathrm{c}} \cdot \mathbf{NN'} - \nabla p_P^{\mathrm{c}} \cdot \mathbf{PP'} \right) \end{aligned} \tag{B.17}$$

Note that, the last of source term $b_P^{p'}$ in the equation above is neglected for SIMPLE. After solving the pressure correction equation, velocity field, pressure field, and mass flow rate at cell interfaces can be corrected with equations, (B.2), (B.3) and, (B.7) respectively. Additionally, for the correction of pressure field, an under-relaxation factor α_{p} is required for the stability purposes. Hence, eq. (B.3) becomes:

$$p = p^* + \alpha_p p^{\mathrm{c}} \tag{B.18}$$